Old Dominion University

ODU Digital Commons

2024

Contribution of High Turbidity to Tidal Dynamics in a Curved Channel in Zhoushan Islands, China

Li Li
Zhejiang University

Fangzhou Shen
Zhejiang University

Zhiguo He
Key Laboratory of Offshore Geotechnical and Material Engineering of Zhejiang Province, Zhoushan, People's Republic of China

Gangfeng Ma
Old Dominion University, gma@odu.edu

Jiachen Wang
Zhejiang University

See next page for additional authors

Follow this and additional works at: https://digitalcommons.odu.edu/cee_fac_pubs

Part of the Geomorphology Commons, and the Transportation Engineering Commons

Authors

Li Li, Fangzhou Shen, Zhiguo He, Gangfeng Ma, Jiachen Wang, and Kailong Huangfu

Taylor & Francis
Taylor & Francis Group

Contribution of high turbidity to tidal dynamics in a curved channel in Zhoushan Islands, China

Li Li[a,b], Fangzhou Shen[a], Zhiguo He[a,b], Gangfeng Ma[c], Jiachen Wang[a] and Kailong Huangfu[a]

[a]Ocean College, Zhejiang University, Zhoushan, People's Republic of China; [b]Key Laboratory of Offshore Geotechnical and Material Engineering of Zhejiang Province, Zhoushan, People's Republic of China; [c]Department of Civil & Environmental Engineering, Old Dominion University, Norfolk, USA

ABSTRACT

The curved tidal channel, Luotou Deep-water Navigational Channel, is the main channel of the Ningbo Zhoushan Port, which is ranked first in the world. Tidal dynamics in the channel are spatially and temporally asymmetric. In this study, the three-dimensional tidal dynamics in the channel were analyzed using field data and simulated using FVCOM. The results show that the tides in the channel flood/ebb along the northern/southern bank near the bottom/surface layer and these asymmetries are due to the imbalanced Coriolis force, centrifugal force, sea-level gradient, and density gradient. Residual current velocity peaks (0.7 m/s) in the middle of the channel as the same distribution as sediment flux. There are two high turbidity zones ($> 4\,\text{kg/m}^3$) which are northern at flood than at an ebb in the channel. The drag reduction effect of fluid mud enhances the lateral circulation, which is strong near the Chuanshan Peninsula and frictional dissipation plays an important role in it. The presence of suspended sediment changes the contribution of acceleration terms through impacting density and bottom friction, and the centrifugal force term has the largest increases. This study provides the foundation for the morphology evolution and harbor management of macro-tidal turbid coastal zones.

Highlights

(1) A baroclinic model was built to study the tidal dynamics in macro-tidal turbid Zhoushan Islands.
(2) Asymmetric tides and lateral circulation occur in the Luotou Deep-water Navigational Channel (DNC).
(3) Mechanism of lateral circulation depends on tidal phases and locations in the DNC.
(4) Sediment impacts water density and drag coefficient, and then changes currents and sediment fluxes in the DNC.

1. Introduction

Tidal dynamics in archipelagoes are complicate and are highly correlated with the local geomorphology and water environment (Choo & Kim, 2013; Wei et al., 2023; Wu et al., 2018). Because of the presence of islands, the tidal dynamics is complex due to spatial variations in water depth and curved topography. High turbidity in archipelagoes impacts the evolution of morphology and variation of water density, and then changes tidal dynamics.

In macro-tidal coastal zones, tidal dynamics in archipelagoes are the dominant factor for the water environment. The tidal circulation around the multiple islands may trap sediment in turbidity maxima (Cancino & Neves, 1999; Wang, He et al., 2022), and may alter the location of turbidity maxima (Kim & Voulgaris, 2008). The ETM (Estuarine Turbidity Maximum) typically occurs near the upriver limit of salt intrusion of macro or mesotidal estuaries, and its position and extent are influenced by tidal oscillations and freshwater discharge (Postacchini et al., 2023). Flood tides carry more fine sediment towards the landward direction compared to ebb tides, leading to the accumulation of fine particles near the coast (Du et al., 2022; Mitchell, 2013).

Interactions between alongshore and cross-shore tidal currents play an important role in cross-shore sediment transport. Therefore, tidal pumping is commonly considered the primary mechanism driving the migration of the ETM in strong-tidal estuaries (Du et al., 2022; Yu et al., 2014). Changes in estuarine flow and extreme climatic events can cause seasonal shifts in the ETM. When freshwater discharge is low, the ETM moves upstream, whereas with higher freshwater discharge, the ETM moves seaward (Dai et al., 2013; Mitchell, 2013), resulting in higher suspended sediment concentrations (SSC) inside the mouth of the Yangtze River during the dry season and lower during the wet season, with the opposite pattern outside the mouth of the river (Dai et al., 2013). Upstream dams and ENSO events have impacts on the position of ETM and SSC within the estuary (Zhou et al., 2020). In microtidal estuaries, storm events can lead to the temporary appearance of the ETM, with higher turbidity values during weaker storm periods and lower turbidity values during stronger storm periods (Postacchini et al., 2023). In general, the SSC within the ETM does not exceed a few hundred milligrams per liter, but the unique topography of the Humber estuary system results in concentrations much higher than this value (Mitchell, 2013). Cross-shore circulation formed within curved river channels influences sediment transport within the river, tending to be scoured by concave banks and silted by convex banks. (Kim & Voulgaris, 2008; Tao & Zhu, 2022). Low velocity zone or eddy current zone will be formed at the back of the island (the wake flow zone), which will lead to the settlement or suspension of sediment (Calil et al., 2008; Isoguchi et al., 2009).

In turbid coastal seas, sediment dynamics in archipelagoes are subjected to and positive feedback to tidal dynamics and geomorphology. The mechanism of sediment transport determines the evolution of shoreline, deposition or erosion of channels and the generation of turbidity zone (Jiang et al., 2013; Wang, Dijkstra et al., 2022), and then feeds back to the tidal dynamics. Sediments change the water density and viscosity (Winterwerp, 2001), and then alter the tidal dynamics, e.g. lateral circulation and stratification (Cheng, 2007).

Curved tidal channels in archipelagoes enhance the complexity of the tidal dynamics and sediment dynamics. Curved channels may have a choking effect on tides, which will inhibit the tidal flow (Byun et al., 2004; Gusti et al., 2023). Generally speaking, axial flow is dominant; while lateral circulation may have a comparable scale (Winant, 2007). Strong lateral circulations can be generated by the asymmetric cross-channel sea level gradients of the curved channel caused by centrifugal force and baroclinic gradient force (Kim &

Voulgaris, 2008; Zheng et al., 2022). Lateral circulation is also affected by other factors, such as nonlinear advection, Coriolis force, and friction dissipation (Xiao et al., 2019).

The Zhoushan Islands (29°32′ −31°04′N, 121°31′ −123°25′E), the largest archipelago in China, is comprised of 1390 islands. It is located in the mouth of Hangzhou Bay (Figure 1(a)). The area has multiple islands, Luotou Deep-water Navigation Channel (DNC) with distinct curvature (Figure 1(c)). The Luotou DNC is the main DNC of Zhoushan-Ningbo Port, and is aligned in an east-west direction. It is the main tidal channel between Hangzhou Bay and the East China Sea (Chen et al., 1990; Figure 1(c)). The channel is about 17 km long and 1.6 km–4.5 km wide, with depths ranging from 35 m to 112 m, which is twice the depth of the surrounding waters (Figure 1(c)). Tides propagate from the outer sea into Hangzhou Bay through the Luotou Channel and the multiple tidal channels between the islands. The tides in the island's sea areas are strong with a large tidal range, strong tidal currents and thorough mixing. The average tidal range reaches 2.5 m, increasing gradually to 4–6 m upstream in Hangzhou Bay (Pan et al., 2019). The sediment transport in the Luotou DNC corresponds to the ebb and flood tidal channels. The suspended sediment concentration decreases during flood tides and increases during ebb tides. The net sediment transport direction is by the ebb tides (Feng & Yao, 2013). Tidal and sediment dynamics in the DNC attack lots of attention, as they are correlated with the siltation and erosion of navigational channels and coastal structures in the Zhoushan-Ningbo Harbor. For example, researchers paid attention to the tides and tidal asymmetry (Chu et al., 2022), suspended sediment concentration (Du et al., 2021) in the islands sea areas. However, the three dimensional tidal and sediment structures in the area, especially in the macro-tidal turbid DNC, are still needs detailed investigation.

Understanding the tidal dynamics in macro-tidal turbid sea areas in multiple islands and their interaction with sediments is important for coastal planning and water quality management. In this study, a three-dimensional numerical model is built and validated, to investigate the tidal and sediment dynamics in the sea area of Zhoushan Islands, with special attention being paid to the tidal structure in the Luotou DNC. Firstly, field observations and numerical simulation methods were used to study the three-dimensional tidal dynamics near Zhoushan Islands. Secondly, the vertical structure of tidal currents/lateral circulation/Eulerian residual currents in the DNC are examined. Thirdly, the impacts of high turbidity on tidal dynamics are numerically investigated.
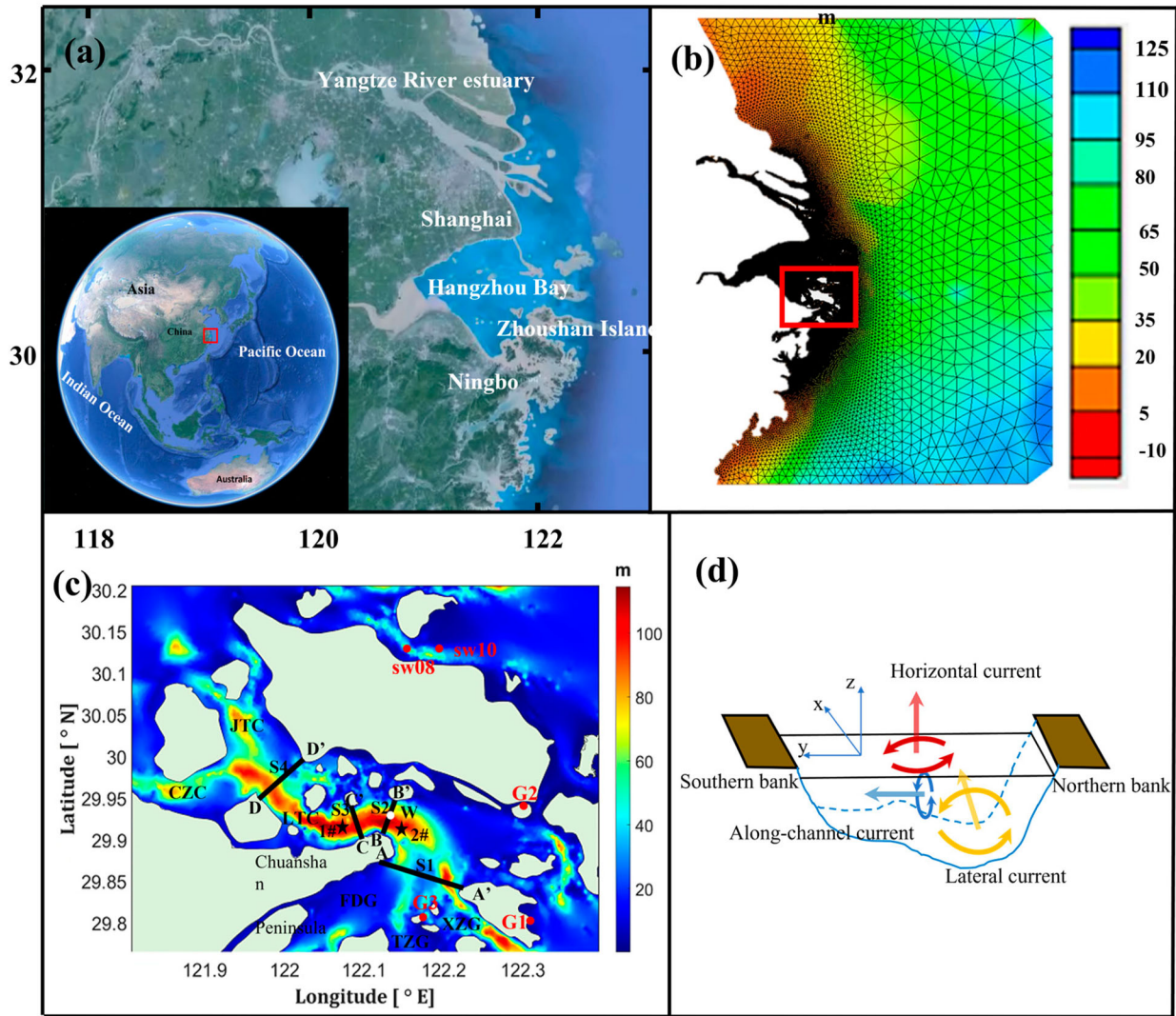
Figure 1. (a) Map of the study area; (b) model grids with depth contours; (c) map of Zhoushan Islands with depth contours, (d) Horizontal/Along-channel/Lateral current direction. Tidal data were collected at Stations G1, G2, G3, respectively. Temperature and salinity data were collected at Stations sw08 and sw10. Stations 1# and 2# were the validation points of current. Sections S1 (A-A'), S2 (B-B'), S3 (C-C') and S4 (D-D') are used to examine the vertical profiles of tidal flow in the Luotou Channel. LTC: Luotou Channel, JTC: Jintang Channel, CZC: Cezi Channel, FDC: Fodu Channel, TZG: Tiaozhoumen Channel, XZG: Xiazhimen Channel.

2. Methodology

2.1. Model description

The hydrodynamic model was built based on the three-dimensional numerical model FVCOM (The Finite Volume Coastal Ocean Model) (Chen et al., 2003). The sediment model was two-way coupled with the hydrodynamic model.

Based on the high turbidity in Hangzhou Bay, the sediment model considers the coupling of the sediment and water density. We use the formula proposed by Winterwerp (2001) to calculate the density of seawater when sediment contributions are taken into account:

$$\rho = \rho_w + \left(1 - \frac{\rho_w}{\rho_s}\right) C$$

where ρ_w represents the seawater density without sediment, ρ_s represents the density of sediment.

Considering the effect of fluid mud, the Flux Richardson number R_f is introduced into the calculation formula of the bottom friction coefficient C_d. The effect of the fluid mud layer on the bottom boundary layer is generalized (Wang, 2002; Wang et al., 2005):

$$C_d = \frac{\kappa^2}{(1 + AR_f)^2 \left[\ln(\frac{h}{z_0} + 1) - 1\right]^2}$$

where $A = 5.5$ is the empirical coefficient, κ is the Karman constant, z_0 represents the bed roughness height and h is the depth.

Consider the effect of flocculation settlement, the model adopts the formula of sediment flocculation settling rate proposed by Cao and Wang (1994):

$$w_s = w_{s0}\frac{1 + c_2 C^{m_2}}{1 + c_1 U^{m_1}} \times k_s$$

where w_{s0} is the settling velocity calculated by the Stokes settling formula, U is the current velocity, c_1, c_2, m_1, m_2, k_s are the empirical coefficient.

The detailed governing equations and numerical methods are presented in the supplementary file.

2.2. Model domain and configuration

The model domain covers the entire Zhoushan Islands and the continental shelf of the East China Sea, including the multiple-island geometry and accurate open-ocean. The unstructured triangular model grid contains 113,704 cells and 61,016 nodes (Figure 1(b)), and the mesh of the main study area (near the Luotou Channel and Zhoushan Islands) is refined and improved to focus on the detailed tidal and sediment dynamics in the DNC, with a resolution of 200 m.

The open boundary of the model is located in the open ocean away from the coast (Figure 1(b)). The forcing on the open boundary includes the main eight tidal components, M_2, S_2, N_2, K_2, K_1, O_1, P_1 and Q_1. These tidal constituents were obtained from the TPXO website (Egbert et al., 1994). The model was run for 14 days from 21th October 2020. For the river discharge of Qiantang River and Yangtze River, refer to the 'China River Sediment Bulletin' (http://www.mwr.gov.cn/sj) The model configuration is shown in the Table 1. The baroclinic effect is considered in the model, the sediment, temperature and salinity affect the density and the bottom friction, and thus the tidal circulation. Hence, sediment, temperature, and salinity are also verified in the model validation. Please see the supplement for a detailed model configuration.

The suspended sediment in the water body has an important influence on the hydrodynamics, especially in high turbidity sea areas, such as in Zhoushan Islands. We set up two cases, without (the reference test 1) and with (test 2) considering sediment, to examine the impacts of high turbidity on tidal dynamics. In test 2, the sediment model is considered, while other settings are the same in test 1 (Table 1).

2.3. Model validation

The model results are validated by hourly tidal-elevation data from two stations, G1, G2, over the period 19th–27th July 2007, and hourly current data from station 1# in 11th–12th and 19th–20th November 2006 and station 2# in 26th–27th January 2007. These stations are near the main study area (deep-water channel) to prove our model is suitable for deep-water channel. We also have the measured current data and hourly averaged temperature and salinity data at station sw08 and sw10 in 25th October (neap tide)/28th October (medium tide)/1st November (spring tide) to validate the model results. Part of the validation figure are shown in the Figure 2, the others are provided in the supplementary file.

As shown in Figure 2, the model results are in good agreement with the measured tidal level data, and the maximum tidal level deviation is less than 10% of the maximum tidal range (~ 3.5 m). The simulated flow velocity and direction are also in good agreement with the measured results, and the deviation of the maximum flow velocity is less than 30% of the maximum flow velocity (~ 1.8 m s^{-1}). The measured temperature is generally larger than the simulated temperature, and the salinity is smaller than the simulated salinity, but the deviations are within 5%, which proves the reliability of the model. The suspended sediment concentrations of this model have been verified, and provided in the supplementary file (Li et al., 2022 and 2023).
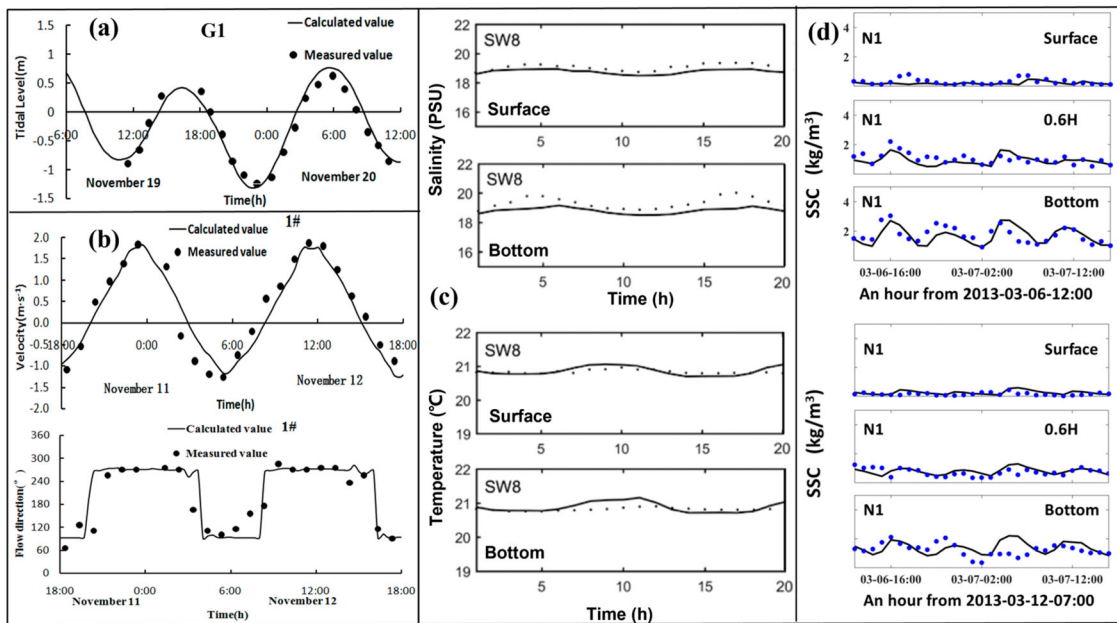
3. Results

3.1. Sea surface elevation in the DNC

The spatial asymmetries in tidal elevation and current velocity are illustrated in the numerical results. Tidal flow in the DNC is characterized by spatially and temporal asymmetric sea surface levels and tidal flow patterns, due to islands and coastlines. The asymmetric characteristics are well reproduced by the numerical model (Figure 3 and Figure 4).

Figure 3(a–d) show the modelled sea surface level during a spring tidal cycle in the DNC. At the high slack water (Figure 3(b)), the sea surface level increases by about 30 cm when tides propagate through the islands from the open sea, due to the nonlinearity and choking effects generated by the multiple islands. The highest sea surface level (about 1.8 m) appears at the west side of the islands. Similar characteristics, with a larger decrease of 40 cm, are found at the low slack water (Figure 3(d)), and the lowest sea surface level (about – 1.4 m) appears at the west side of the islands. At the peak flood/ebb current (Figure 3(a, c)), the sea surface level is about 40 cm

Table 1. model parameter and case configuration.

Model parameter	Parameter setting
Grid resolution	200-30000 m
Number of nodes and elements	61016, 113704
Number of sigma layers	20
Internal and external model time step	2s, 0.2s
Median particle size of sediment	0.008 mm
Sediment porosity	0.5
Sediment settling velocity empirical parameter	0.06, 4.60, 0.75, 0.90, 1.30
Critical incipient motion shear stress	0.1 N m-2
Sediment erosion rate	0.00005-0.0006 kg m-2 s-1
Bed roughness length	0.005-0.05 mm

Case name	Temperature	Salinity	River	Sediment
Test 1	✓	✓	✓	×
Test 2	✓	✓	✓	✓

Figure 2. Comparison of observed and modeled (a) sea surface elevation at Stations G1; (b) current velocity and direction at Stations 1#; (c) temperature and salinity at Stations sw08, (d) SSC at Station N1. Solid lines indicate model results; dotted lines indicate observed results.

lower/higher at the landward side than the seaward side of the DNC, due to the choking effect of the DNC.

During the neap tidal cycle (Figure 3(e–f)), the tidal elevations are more asymmetric spatially at high and low slack water in the DNC than during spring tides. At slack water (Figure 3(f, h)), the decrease of sea surface level (by about 10 cm) is smaller than that during spring tides, when the tides propagate through the islands, again due to the nonlinearity and choking effects generated by the multiple islands. At the peak flood/peak ebb current (Figure 3(e, g)), smaller difference (20 cm) of sea surface levels between seaward and landward sides of the DNC happens during neap tides than that during spring tides.

During flood tides, the Coriolis force is in the same direction with the centrifugal force, towards the bank opposite the cusp of the Chuanshan Peninsula, indicated

by 'C' in Figure 3(a). Hence the tidal flow near the cusp shows a spatially asymmetric pattern (Figure 3(a)), which means the sea surface level is lower near the peninsula cusp and becomes higher at the opposite bank. During ebb tides (Figure 3(c)), the Coriolis and the centrifugal forces are in opposite directions, and the flow pattern is less asymmetric.

The tidal flow near the surface and bottom levels are shown in Figure 4. During spring tides (Figure 4(a–d)), the tidal current directions around the Zhoushan Islands are basically in accordance with the coastlines. The main flow channel is from the head of the Chuanshan Peninsula, through the DNC to the Cezi and Jingtang channels, and finally into Hangzhou Bay (Figure 1). The velocity of ebb tides is higher than that of flood tides. The flow is near the southern bank of DNC during ebb tides, while is near the northern bank during flood tides. The flow channel
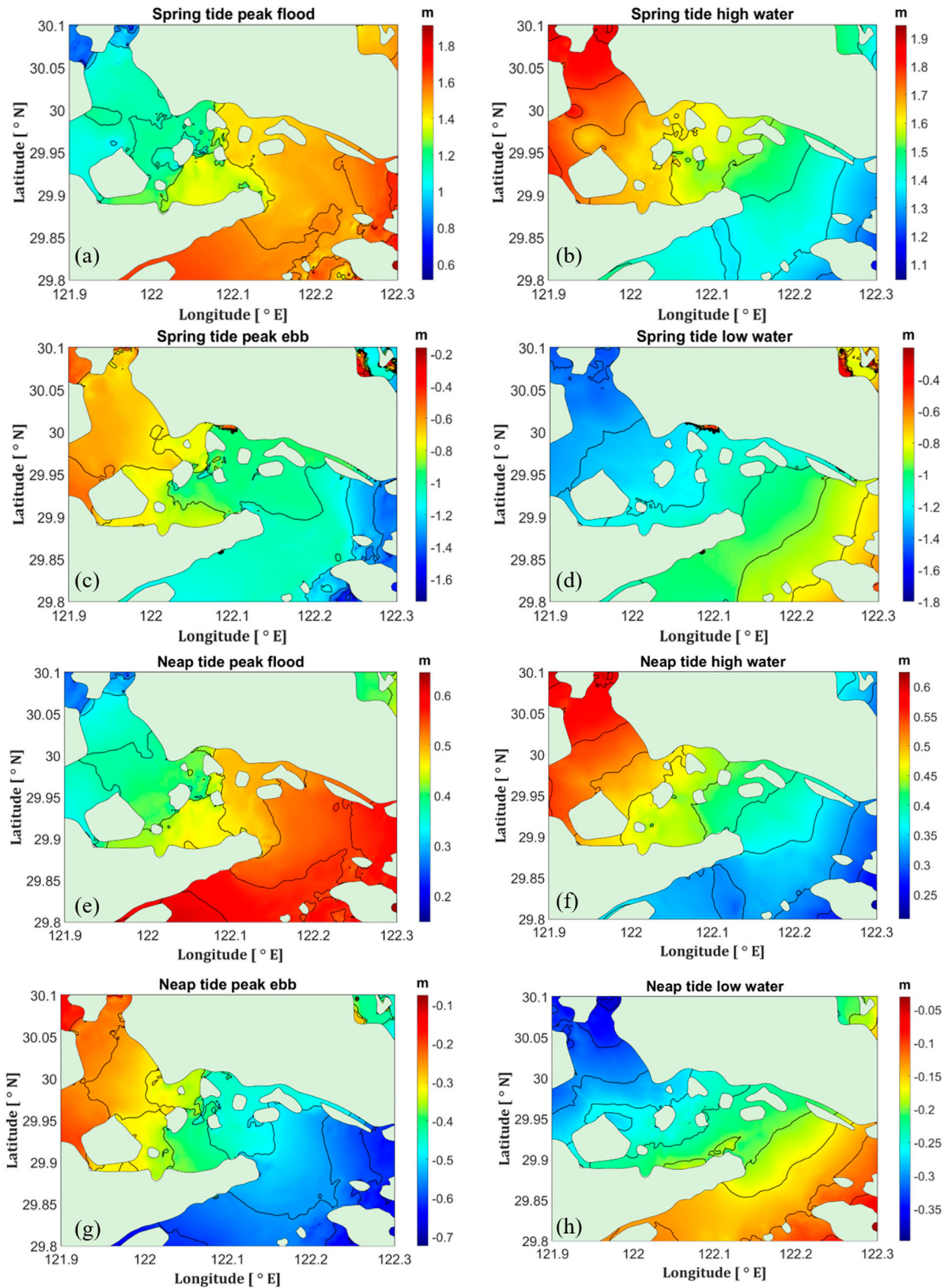
Figure 3. Modeled instantaneous sea surface level in the channel in a spring tidal cycle: (a) peak flood; (b) high slack water; (c) peak ebb; (d) low slack water. (e-f) are the same as (a-d), but for a neap tidal cycle.
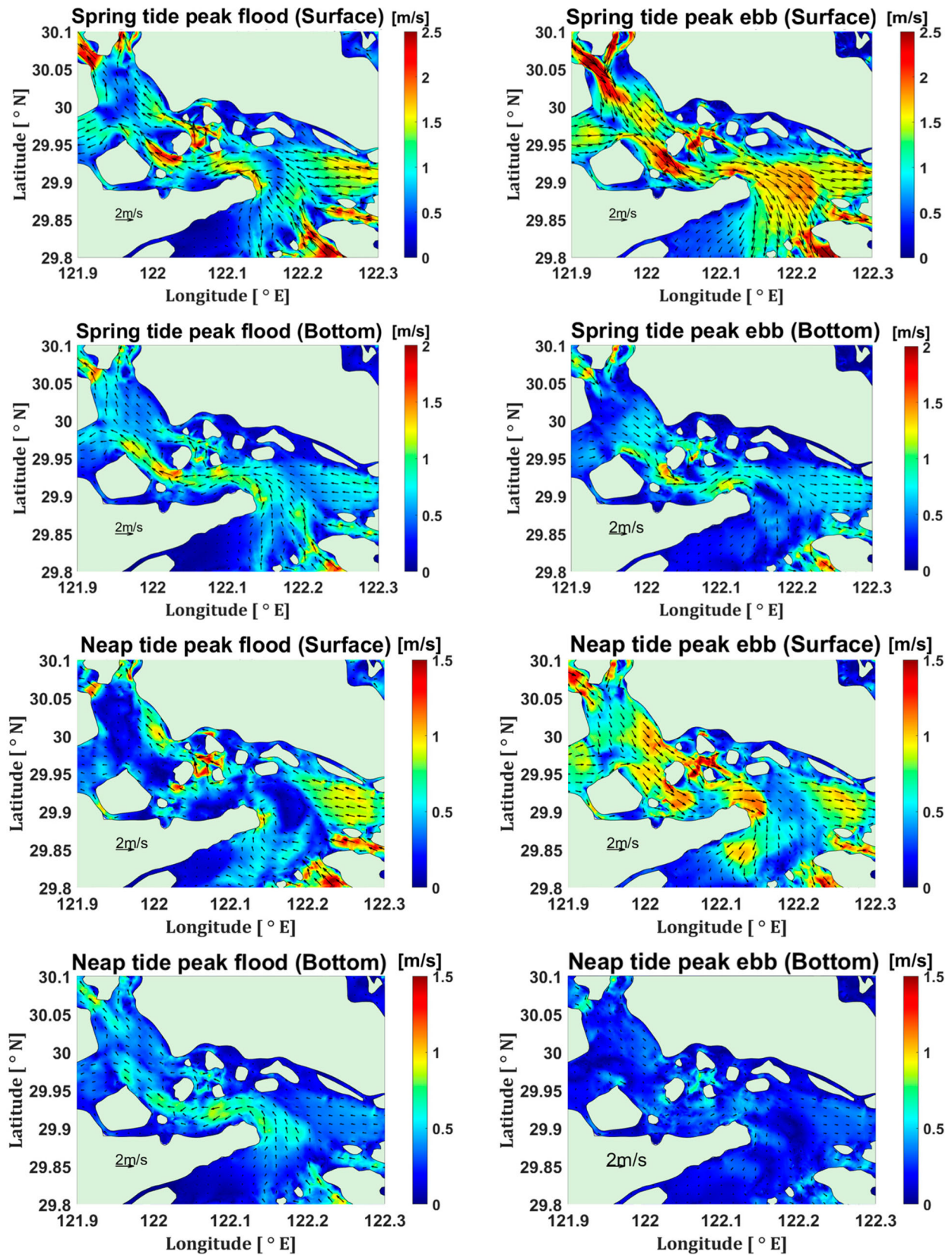
Figure 4. Modeled instantaneous tidal flow of the surface/bottom layer during a spring/neap tide.

at the seaward entrance of the DNC is more curved at the bottom level than that at the surface during both peak flood and ebb currents, due to the impact of the islands. Eddies occur (in the horizontal x-y plane) around the islands, only at slack waters during both flood and ebb tides. During peak flood and peak ebb tides, tidal flow is homogeneous, with wake flows near the islands.

Weaker tidal forcing during neap tides (Figure 4(e–f)) led to weaker current velocities during flood and ebb tides. Similarly, the strength of the ebb flow is greater. Compared with the spring tides, the flow is more curved in some area due to the smaller velocity. In addition, the low velocity zone behind the island (wake flow zone) decreases due to the low flow velocity.

3.2. Vertical structure of tidal currents in the DNC

The flood and ebb tidal current velocities and vectors at 1, 12, 30 and 60 m below the sea surface during a spring tide are shown in Figure 5. These depths were chosen because the 1 m depth is in the near-surface level, the 12 m depth is the mean depth in this vicinity, and the 30 and 60 m depths are located lower down in the DNC.

The current velocity decreased from about 2.0 m s^{-1}/2.2 m s^{-1} at the 1 m level (Figure 5) to about 1.8 m s^{-1}/1.8 m s^{-1} at the 60 m level in the DNC at the flood/ebb current during spring tides. The peak current velocities occur at the northern bank of the Luotou Channel during the flood current and the south bank during the ebb current due to the effects of the Coriolis force. The vertical current-velocity gradients are larger during flood tides than ebb tides.

At a depth of 30 m in the DNC (Figure 5), tides come in mainly through the Tiaozhoumen and Xiazhimen Channels (Figure 1(c)), with peak current velocities at the Xiazhimen Channel. Tides move out from Hangzhou Bay to the DNC through the Cezi and Jintang channels, with peak current velocities occurring in the Jingtang Channel. The horizontal tidal currents are complex through the islands near the northern bank of the DNC, affecting the current velocity in the DNC.

There is a similar flow pattern at 60 m with that at 30 m, but with no currents outflow to or inflow from the islands near the northern bank of the DNC, due to the water depth. Hence, the flow in the DNC at this depth is quite homogeneous and is constrained within the DNC, with slight variations due to bathymetry changes.

3.3. Lateral circulation at cross-sections in the DNC

To examine lateral circulations in the DNC, cross-sections S1, S2, S3 and S4 (Figure 1(c)) were selected to illustrate the vertical profiles of tidal current velocities. For the convenience of representation, we define the velocity perpendicular to the section direction as V_x, the velocity along the section direction as V_y, and the velocity along the water depth direction as V_z. Positive values indicate the eastward, northward and upward directions.

Section S1 is at the southern entrance to the channel. The tidal current, flooding into the channel from the outer sea, has peak along-channel velocity V_x at the surface layer at the eastern bank (1.2 m s^{-1}) (Figure 6(a)). The vertical gradient of flow velocity is small in the deep channel on the eastern bank. On the west side of the section, there is a weak circulation (V_y, the third-row arrow). During ebbing from the channel to the outer sea, the along-channel tidal current velocity V_x also peaks at the surface layer with a velocity of 1.2 m s^{-1}, on the middle and eastern side of the channel (Figure 6(b)). There is a large lateral circulation (V_y) near the deep channel on the eastern bank of the Section S1. Opposite currents on the western bank also create lateral circulation (V_y, the second to fourth-row arrow). The lateral flow of section S1 is mainly northward/southward at the peak flood/ebb tides, and the surface/bottom flow velocity is high/low. The lateral flow velocity reaches the maximum (1.3 m s^{-1}) on the surface of the middle channel.

At Section S2 (Figure 6(c–d)), the peak flood and ebb current velocities V_x are higher at the southern bank (1.6 m s^{-1} and 1.5 m s^{-1}) than at the northern bank (1 ms^{-1} and 1 m s^{-1}). There is a lateral circulation, with surface currents towards the northern bank (0.9 m s^{-1}) and bottom currents towards the southern bank (0.5 m s^{-1}) (Figure 6(c)) at the peak flood tide. At the peak ebb tide, water flows almost exclusively from the northern bank to the southern bank, except for a small circulation on the northern bank. The maximum flow velocity (0.6 m s^{-1}) is almost in the middle of the water instead of the surface. Because the surface water has a northward flow trend in the action of centrifugal force.

Tides flood through Section S3 (Figure 6(e)) along the northern bank (peak current velocity V_x 1.8 m s^{-1}) and ebb (Figure 6(f)) along the southern bank with a peak current velocity of about 1.4 m s^{-1}. During the flood tides, no strong lateral circulation occurs, with only some surface water flowing in the south direction. The water flows mainly from the southern bank to the northern bank, with the maximum velocity (0.5 m s^{-1}) in the middle of the water. Strong lateral circulation appears during the ebb tides, with surface currents (0.6 m s^{-1}) towards the southern bank and bottom currents (0.3 m s^{-1}) towards the northern bank.

Section S4 connects the DNC with Hangzhou Bay. Current floods along two main tidal channels into Hangzhou Bay (Figure 6(g)), with peak current velocity

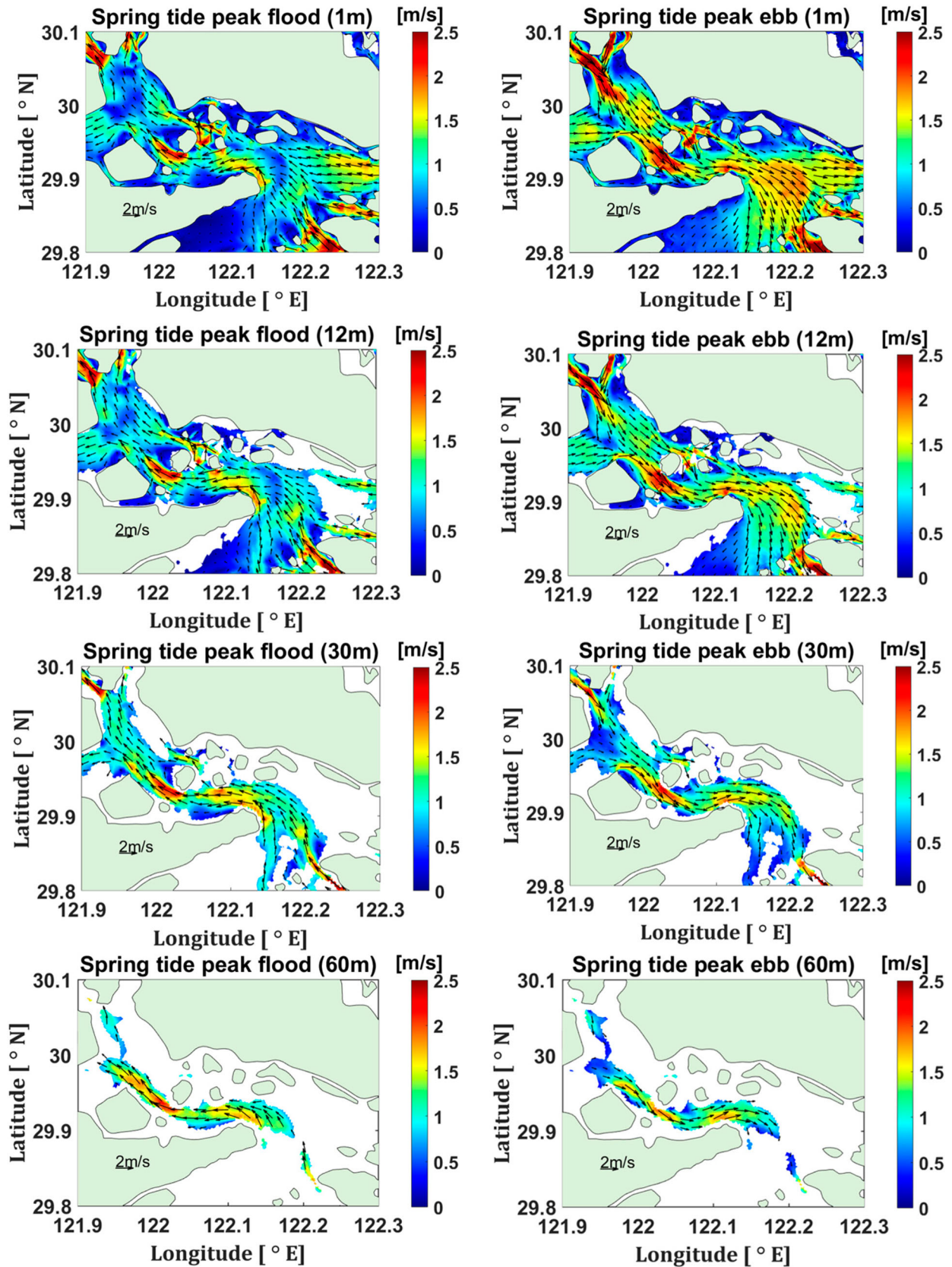**Figure 5.** Modeled tidal flow during a spring tide at: (a) peak flood and (b) peak ebb tide at 1 m below the surface; (c) peak flood and (d) peak ebb tide at 12 m below the surface; (e) peak flood and (f) peak ebb tide at 30 m below the surface; (g) peak flood and (h) peak ebb tide at 60 m below the surface. The depths are those at Station M for peak flood tides and Station N for peak ebb tides.
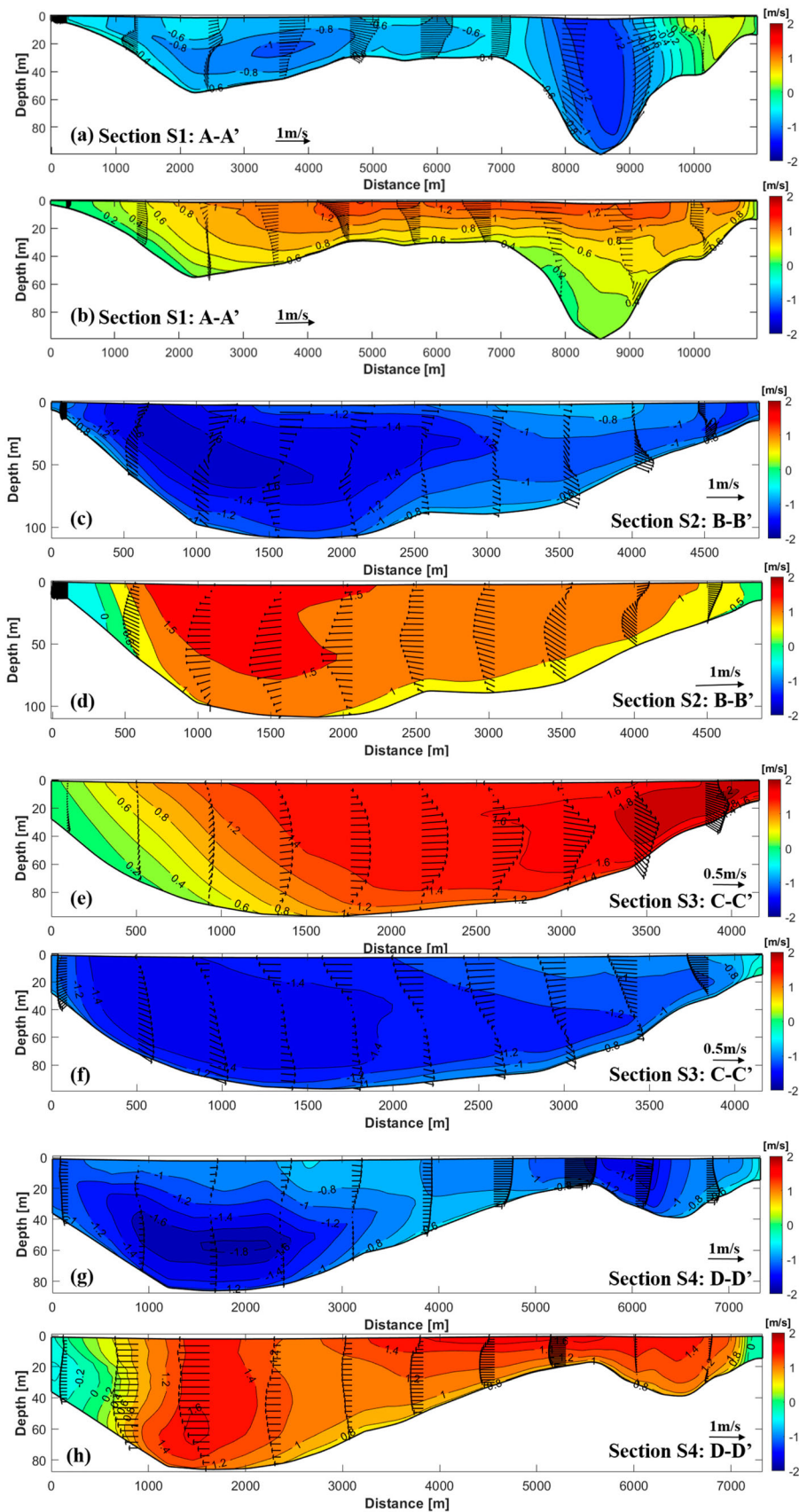
Figure 6. Modeled cross-sectional current velocities during spring tides at Section S1: (a) peak flood and (b) peak ebb current; (c, d), (e, f) and (g, h) are same as (a, b), but for Section S2, S3 and S4, respectively. Color contours indicate the current velocity perpendicular to the section direction as V_x. Arrow indicates the velocity along the section direction as V_y.

16

V_x 1.8 ms^{-1} in the southern channel and 1.4 ms^{-1} in the northern channel. Ebb currents are along the same channels back to the DNC (Figure 6(h)), with peak current velocity V_x 1.6 m s^{-1} in the southern channel and 1.4 m s^{-1} in the northern channel. The southern channel has a larger depth, and the vertical distribution of velocity is similar to the logarithmic distribution. The maximum velocity is at a depth of about 60 m. There is no strong lateral circulation here. The lateral flow is mainly northward (0.9 m s^{-1})/southward (0.9 m s^{-1}) at the peak flood/ebb tides.

According to the above, the lateral flow velocity V_y is of the same order of magnitude as the axial velocity V_x in the curved channel and there are lateral circulations in sections S1 to S4.

3.4. Eulerian residual currents in the DNC

As residual currents are important for sediment and nutrient transport, we calculate the Eulerian residual current velocities in the DNC (Methods are provided in the supplementary file). The calculation duration is a spring-neap tide cycle. The Eulerian residual current velocities at 1, 12, 30 and 60 m below the sea surface and the vertically averaged residual current velocities are shown in Figure 7. The residual current velocities vary by the geometry of the islands, with large current velocities occurring on the Jingtang Channel (0.7 m s^{-1} at 1 m below sea surface), the area around the islands near the DNC (0.8 m s^{-1} at 1 m below sea surface) and northern side of the Chuanshan Peninsula (0.6 m s^{-1} at 1 m below sea surface). The main reasons are the asymmetric ebb and flood tide and the blocking effect of islands (during ebb and flow tide, a wake flow zone with low flow velocity will appear behind the island). At the seaward entrance of the DNC, a clockwise eddy appears (Figure 7) near the western bank (at Section S1, Figure 1(c)) and an anti-clockwise eddy (Figure 7) appears near the eastern bank (at Section S2-S3, Figure 1(c)), with vertically averaged current velocity of about 0.4 m s^{-1}.

Vertically, the residual current decreases or even increases inversely leading to a vertical circulation in the sections S1-S4. Such as there is a vertical circulation in the deep channel on the eastern bank of section S1. Then, we find the lateral circulation clearly on the residual current profile of sections S1 and S2. The upper residual current flows to the southern bank (eastern bank in section S1) and the lower residual current flows to the northern bank (western bank in section S1). This phenomenon is also seen slightly in section S4 but almost none in section S3. There are obvious lateral flows in each section (0.2 m s^{-1} in sections S1, S2, S3 and 0.3 m s^{-1} in S4.) (Figure 8).

3.5. SSC and sediment fluxes in the DNC

In the DNC, it is difficult for sediment to be thoroughly mixed to the surface layer due into the large water depth. The SSC near the bottom layer is 2–4 times greater than that near the surface layer (Figure 9). During spring tides, the sediment at the bottom is re-suspended when flow velocity is large (e.g. peak flood and peak ebb currents), and the maximum SSC reaches $4 \sim 5$ kg m^{-3}; while the maximum SSC at the bottom is about $2 \sim 2.5$ kg m^{-3} during neap tides, due to smaller current velocity. There are two high turbidity zones near the bottom layer (bottom SSC > 4 kg m^{-3}), which are located in the northwest of the Chuanshan Peninsula (HSSC2, Figure 9(g)) and in the channel between the two islands (HSSC1, Figure 9(g)). The location of these two turbidity zones is by the high flow velocity areas (Figure 4). The locations of the surface turbidity zones (surface SSC > 1.5 kg m^{-3} during spring tides) are different from those near the bottom level, due to the lateral transport of sediment. In the position of S2 section, the location of the surface high turbidity zone is more northward at flood tides and more southward at ebbing tides.

The sediment fluxes in unit width (the calculation method is in the supplementary file) in the DNC are smaller in the middle of the channel and larger on both sides during a spring/neap tide. In a neap tidal cycle, due to the low bottom flow velocity, the sediment fluxes are very small at the bottom (although the SSC is very large), and the maximum sediment flux at the surface/bottom reaches 5 kg/15 kg (per neap tidal cycle, unit width, 24 h) near the northern bank of section S3/in the middle of the channel (Figure 10). During a spring tidal cycle, large flow velocity and large SSC lead to a large sediment flux, which reaches 15 kg/20 kg (per spring tidal cycle, unit width, 24 h) near the surface/bottom layer near the northern bank of the channel /in the middle of the channel (Figure 10). Overall, the distribution of sediment fluxes is similar to the distribution of residual currents. From an along-channel perspective, the sediment fluxes are large in the areas with high residual current velocity. The maximum sediment flux occurs near the bottom level because the sediment is scoured from the sea bed and the bottom SSC is much greater than that near the surface. From a lateral perspective, the lateral sediment transport and residual current are almost identical, and the directions of the surface and bottom sediment fluxes are opposite in the sections S1 to S4, due to the lateral circulation.

Seen from the sediment fluxes at each section, there is an obvious asymmetry in sediment transport in the curved DNC. Except for section S2, sediment is
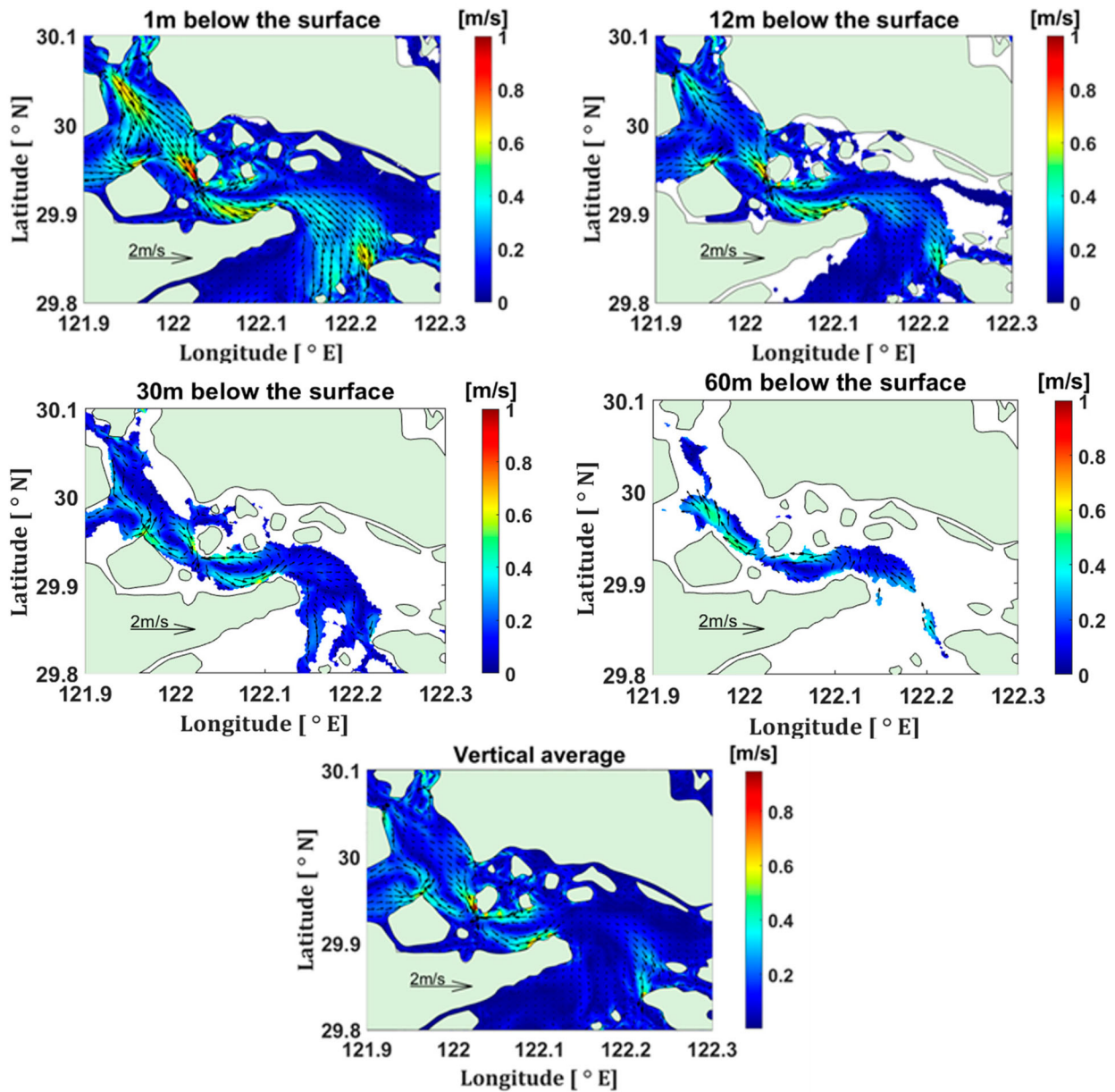
Figure 7. Modeled Eulerian residual current velocities at: (a) 1 m; (b) 12 m; (c) 30 m; (d) 60 m below the surface; and (e) vertically averaged Eulerian residual current velocity.

transported landward along the northern bank of the channel; and seaward alone the southern bank. The section S1 is outside the seaward entrance of the DNC, and has a large width. There are two channels for inward and outward sediment fluxes, and the sediment fluxes are relatively small (-60 kg ~ 100 kg, minimum on the bottom of the western bank, maximum on the bottom of eastern bank). Sections S2-S4 in the DNC have high flow velocity and high SSC, so the sediment fluxes are large, especially in section S3 (in the middle of the DNC, -300 kg ~ 350 kg, minimum on the bottom of the southern bank, maximum on the bottom of the northern bank). At each section, there are large lateral sediment fluxes, up to $80 \sim 140$ kg near the bottom layer. Lateral circulations

of sediment occur in sections, with the sediment fluxes in opposite directions near the surface and the bottom layers (Figure 11).

4. Discussions

4.1. Interaction of Coriolis and centrifugal force on lateral circulation

In a channel with flood and ebb tides, the lateral circulation of centrifugal force in a bend can be broken down into two components, a steady component and a periodic component. It could be reflected in the sea surface elevation, where the steady component maintains a constant
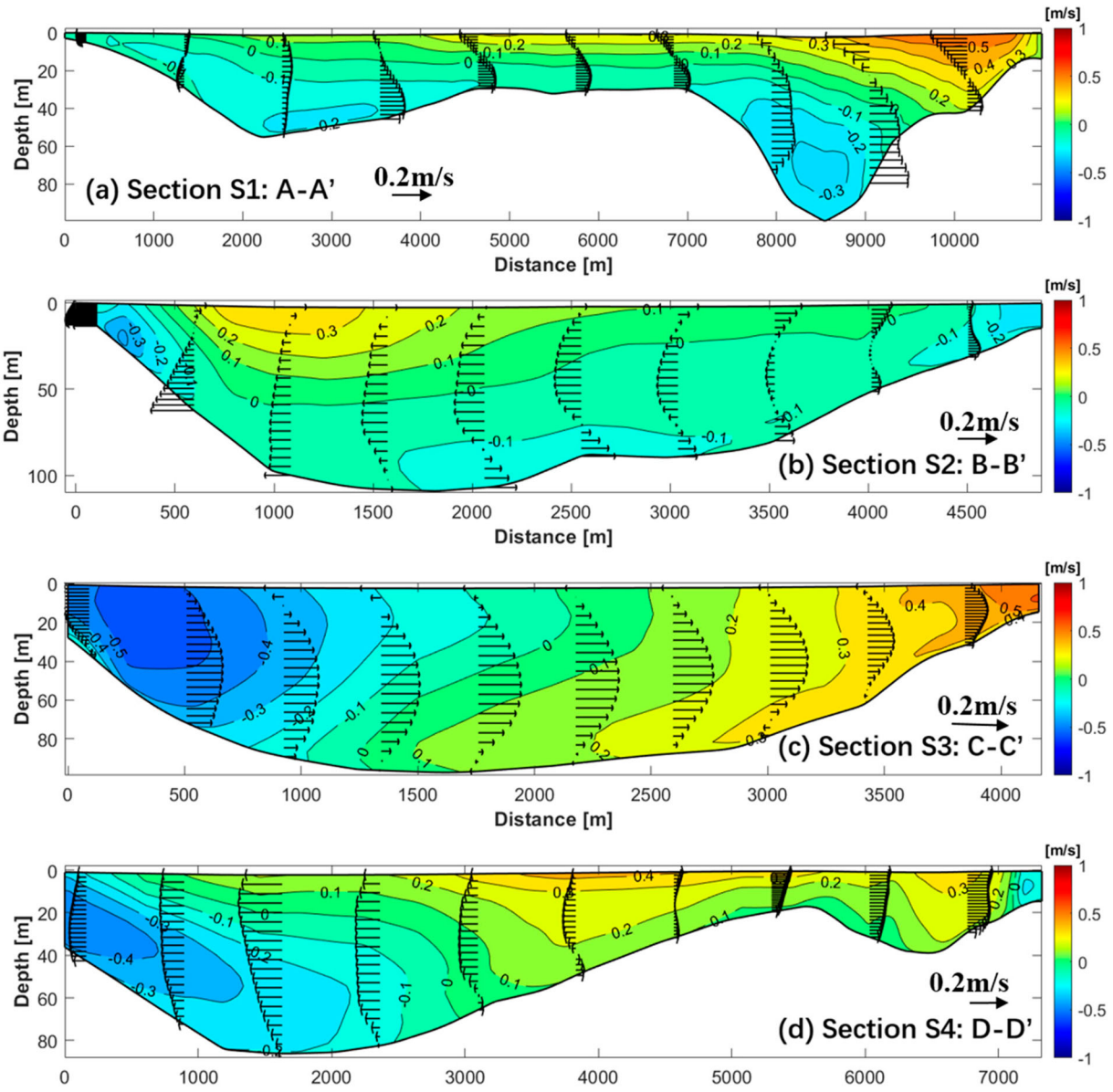
Figure 8. Modeled Eulerian residual current velocities during a spring-neap tide cycle at Section S1-S4.

sea surface gradient, and it changes when the periodic component is superimposed (Cheng, 2023). In this study, the sea level at Section S3 is higher on the south bank than on the north bank at peak ebb. The difference is smaller at peak flood, and it is more pronounced at spring tide because the centrifugal force is related to the flow speed.

The pattern of circulation in Section S2 is induced by the imbalance between the cross-sectional sea-level gradient, the centrifugal force and the Coriolis force in the vertical water column, as the centrifugal force and the Coriolis force vary with current magnitudes. During flood tides, the centrifugal force together with the Coriolis force exceeds the sea-level gradient at the surface level to form a lateral circulation directed to the northern bank in the curved channel, while the converse is true near the bottom (Figure 6(c, d)). Then a clockwise

circulation is formed. During ebb tides, the sea-level gradient is directed to the southern bank, as the centrifugal force is always larger than the Coriolis force (Table 2). Then, the sum of centrifugal force and the Coriolis force overtakes the sea-level gradient at the surface level, while the converse is true near the bottom. Thus, a clockwise circulation is also formed. This flow is expected to play an important role in residual circulation and sediment transport.

The combined effects of the Coriolis and centrifugal forces were examined to specify the spatially asymmetric characteristics of the tidal flow caused particularly by the tides. Due to the Coriolis force, the flood tide is turned to the northern bank of the channel, and the ebb tide is pushed to the southern bank of the channel. The centrifugal force pulls the flow to the northern bank. The
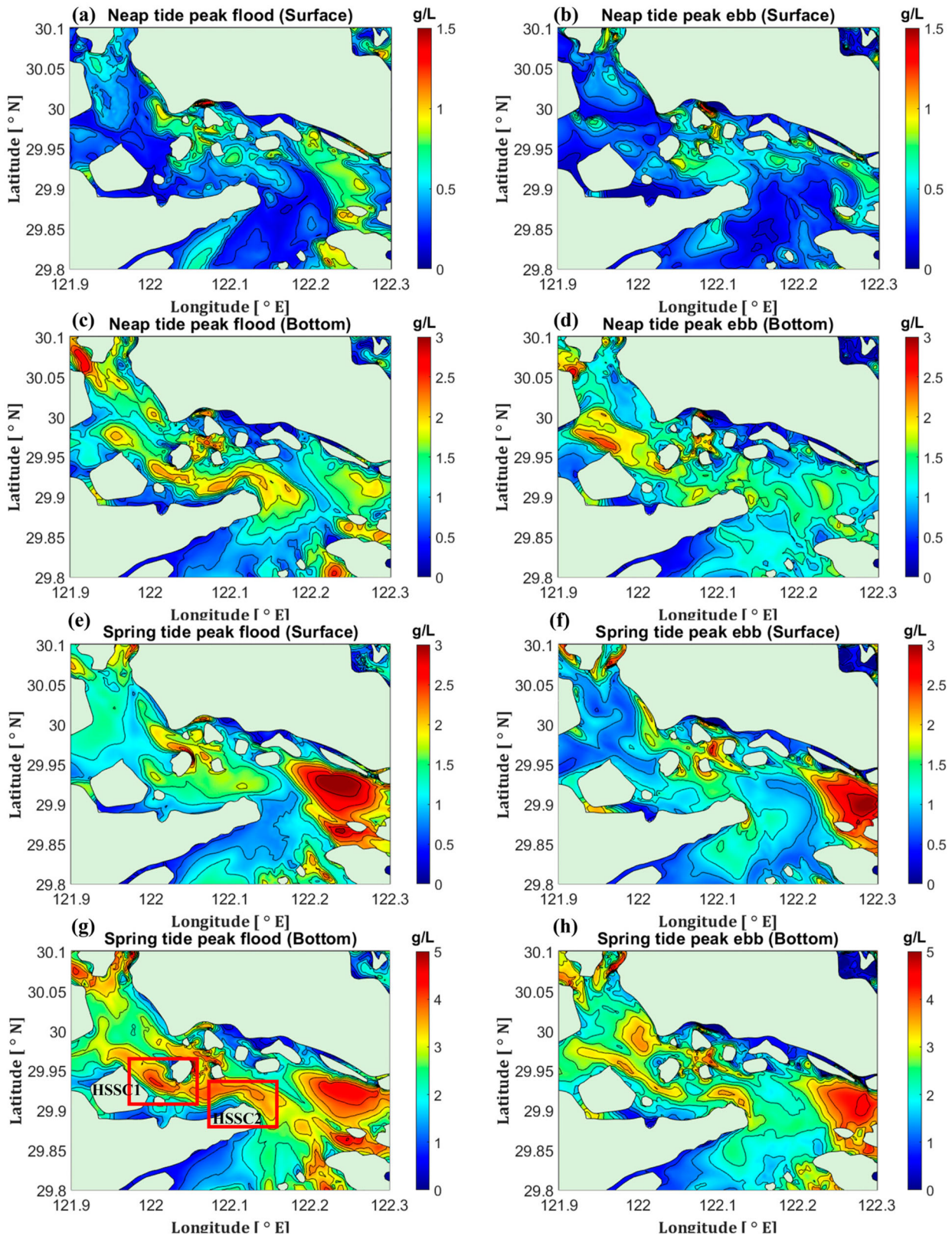
Figure 9. Surface and bottom SSC in the DNC during peak flooding and peak ebbing tides during neap and spring tides.

cross-channel pressure gradient subsequently produces a lateral circulation pattern. The centrifugal forces have the reverse effects. This is consistent with the results mentioned by Cheng (2023). He mentioned the relatively importance of the Coriolis and centrifugal force is measured by Rossby number. Here, we use a more intuitive
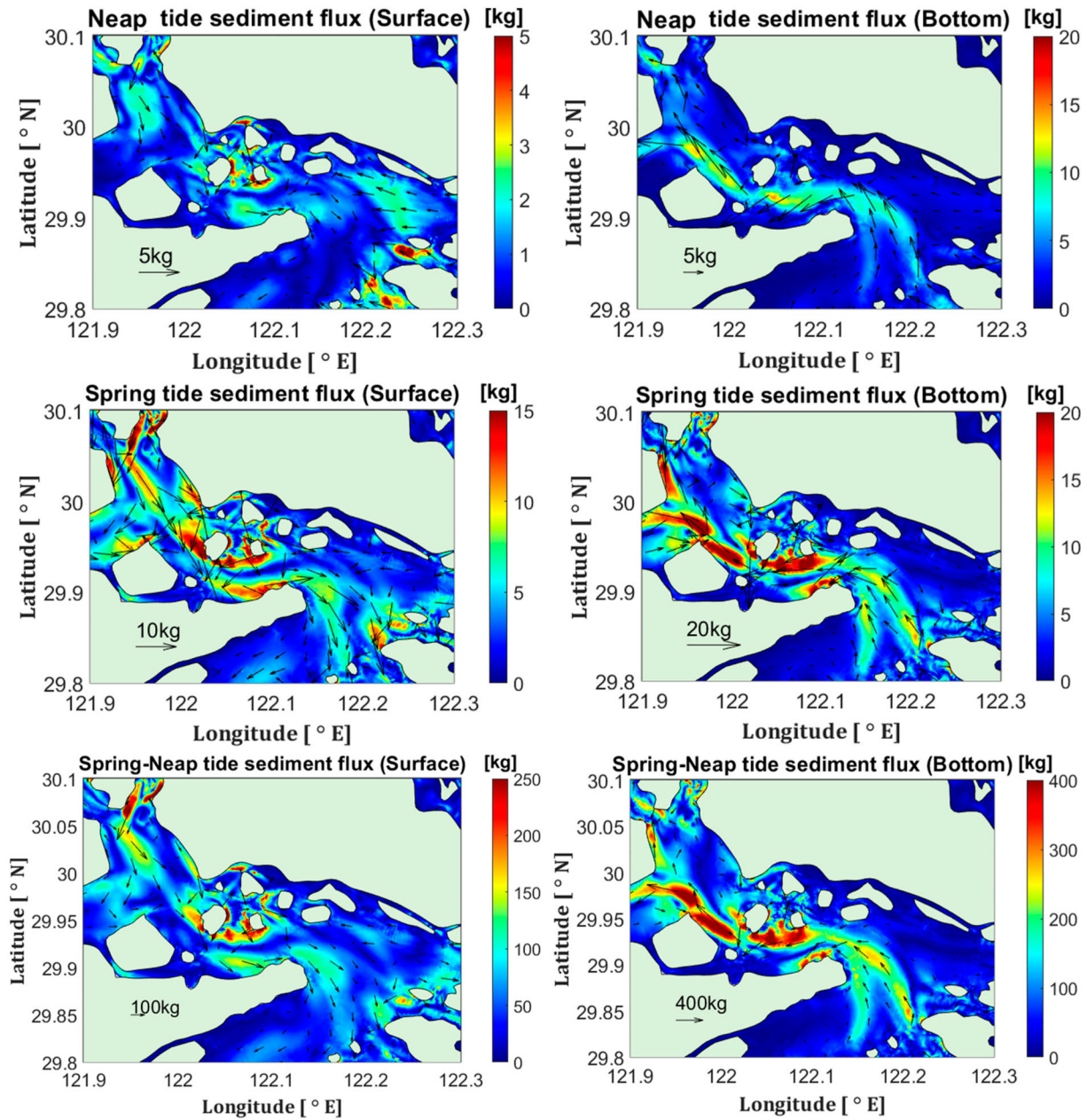
Figure 10. Surface and bottom sediment fluxes in the DNC during a neap tidal cycle, a spring tidal cycle and a spring-neap tidal cycle.

comparison of these two forces along the channel, which is shown in Table 2. The ratio of the centrifugal force to the Coriolis force is 2.1, indicating that the centrifugal force is more important in the DNC. This is due to the curved flow structure and the controlling effect of coastlines. The combined effects of the Coriolis and centrifugal forces also enhance mixing in the channel.

4.2. Impacts of SSC on currents

Figure 12 illustrates the modeled flow velocity in the DNC, when considering the impacts of suspended sediment (test 2). The flow velocity in the DNC is high

at peak flood and ebb currents during spring tides, with current speed of $2.5\,\mathrm{m\,s^{-1}}/1.5\,\mathrm{m\,s^{-1}}$ at the surface/bottom layer. Current speed is relatively low during neap tides. Compared with Figure 4, the presence of sediment increases the flow velocity in DNC during spring tides. During neap tides, the current velocity increases slightly, and even decreases in some areas. Considering the sediments in the model (test 2), the flood tidal channel near the bottom level is moved northward. The influence of the sediment on the flow is calculated (flow velocity in test 2 minus that in test 1) and illustrated (Figure 13). During spring tides, within the DNC, when sediment is considered in the model (test 2), the current
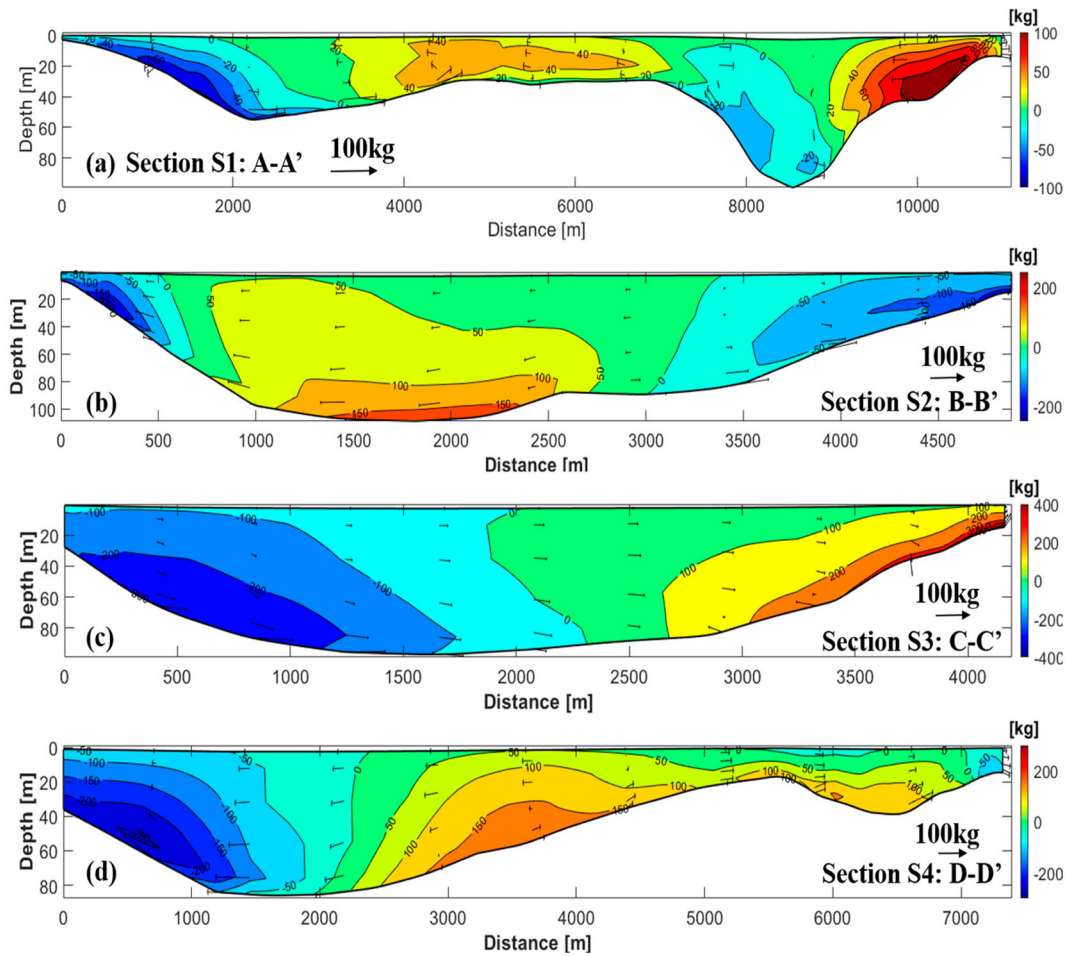
Figure 11. Sediment fluxes at each section during a spring-neap tidal cycle. Color contours indicate along-channel sediment flux (along the channel axis), with positive values representing landward and negative values representing seaward. Arrows indicate lateral sediment fluxes (perpendicular to the channel axis). The horizontal coordinates start from the southern bank of the channel.

Table 2. Comparison of Coriolis force and centrifugal force in the Luotou Channel.

	Coriolis force (m s^{-2})	Centrifugal force (m s^{-2})	Centrifugal/Coriolis
Force	$2\Omega U \sin(\theta)$	U^2/R	$\frac{2\Omega U \sin(\theta)R}{U^2}$
Value	1.1×10^{-4}	2.3×10^{-4}	2.1

*Note: $\Omega = 0.0000729$ s^{-1}; $U = 1.5$ m s^{-1}; $\theta = 29.99°$; $R = 10000$ m;

velocity increases greatly. The increased velocity mainly occurs in the larger SSC area, mainly along the axis direction. Considering the sediment in the model in test 1 also promotes lateral circulation within the DNC. The same phenomenon is seen during neap tides, but the effect issmaller.

Sediment impacts water from two different ways in the numerical model. First, the SSC impacts water density, and creates baroclinic gradient forces that promote current velocity. According to Figure 14, the residual density caused by sediment is up to a maximum of 2 kg m^{-3},

which is a small change relative to the density of the water, and may not be able to make such a large change in flow velocity. The second way, is the drag reduction effect due to the fluid mud in the bottom boundary layer. The sediment particles in Zhoushan Islands are mainly silt, and the mud layer is formed at the bottom level. As early as 1998, Shi (1998) discovered the fluid mud layer at the seabed in Hangzhou Bay. Under the action of oscillatory shear, the mud becomes a fluid stage after 'two-step' yield, and the apparent viscosity and complex viscosity of the mud are greatly reduced (Wang, He et al., 2022). It means the presence of the mud layer reduces the C_d value, and subsequently dampens the bottom stress, so that the flow velocity changes. Hence, we use the optimized C_d to represent the drag reduction effect of fluid mud layer (Yao et al., 2023). The fluid mud layer will persist under continuous hydrodynamic conditions and become thicker under strong hydrodynamic conditions (such as typhoon) (Wu et al., 2023).
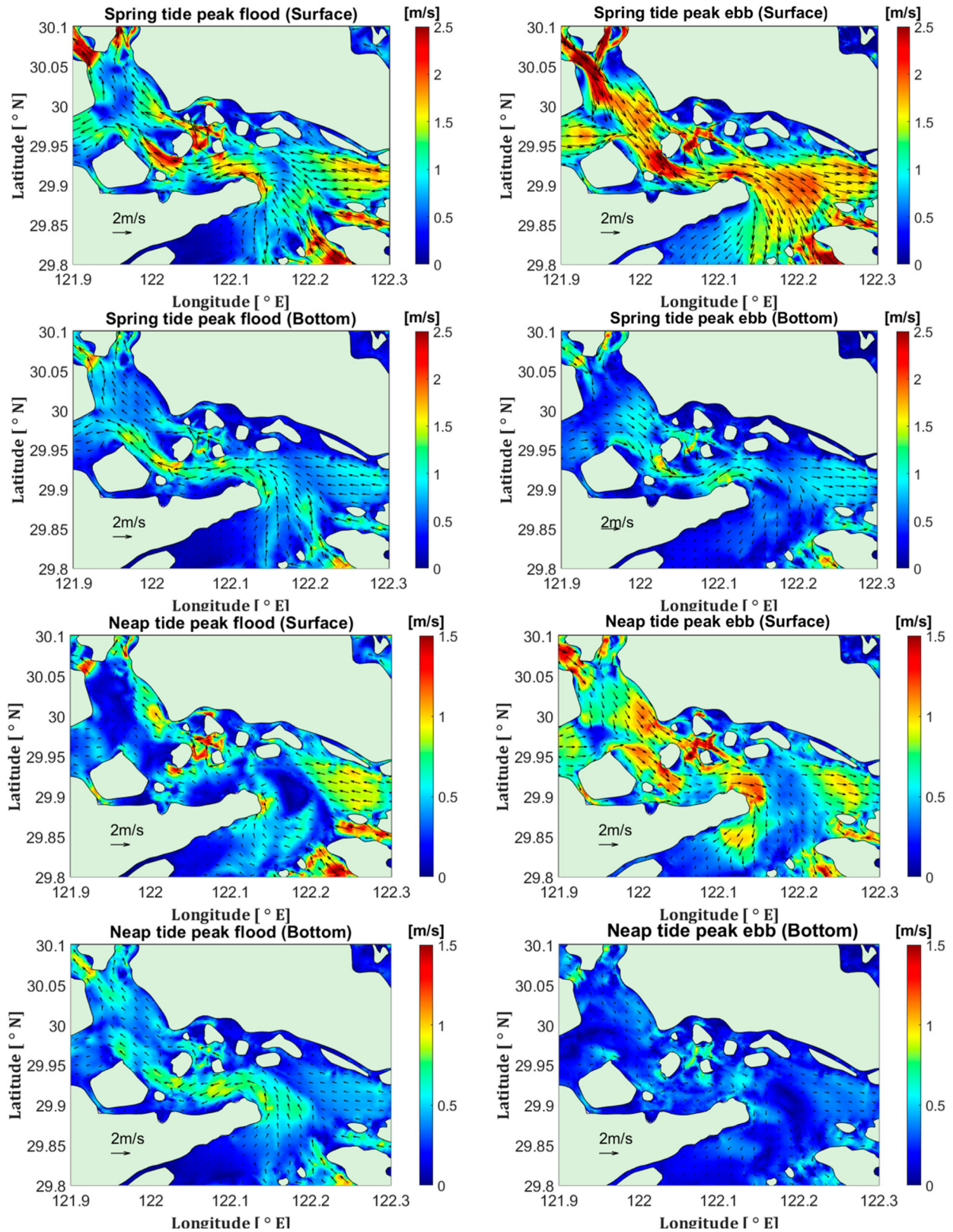
Figure 12. Modeled tidal flow near the surface/bottom layer during spring/neap tides when considering sediment in the model (test 2).
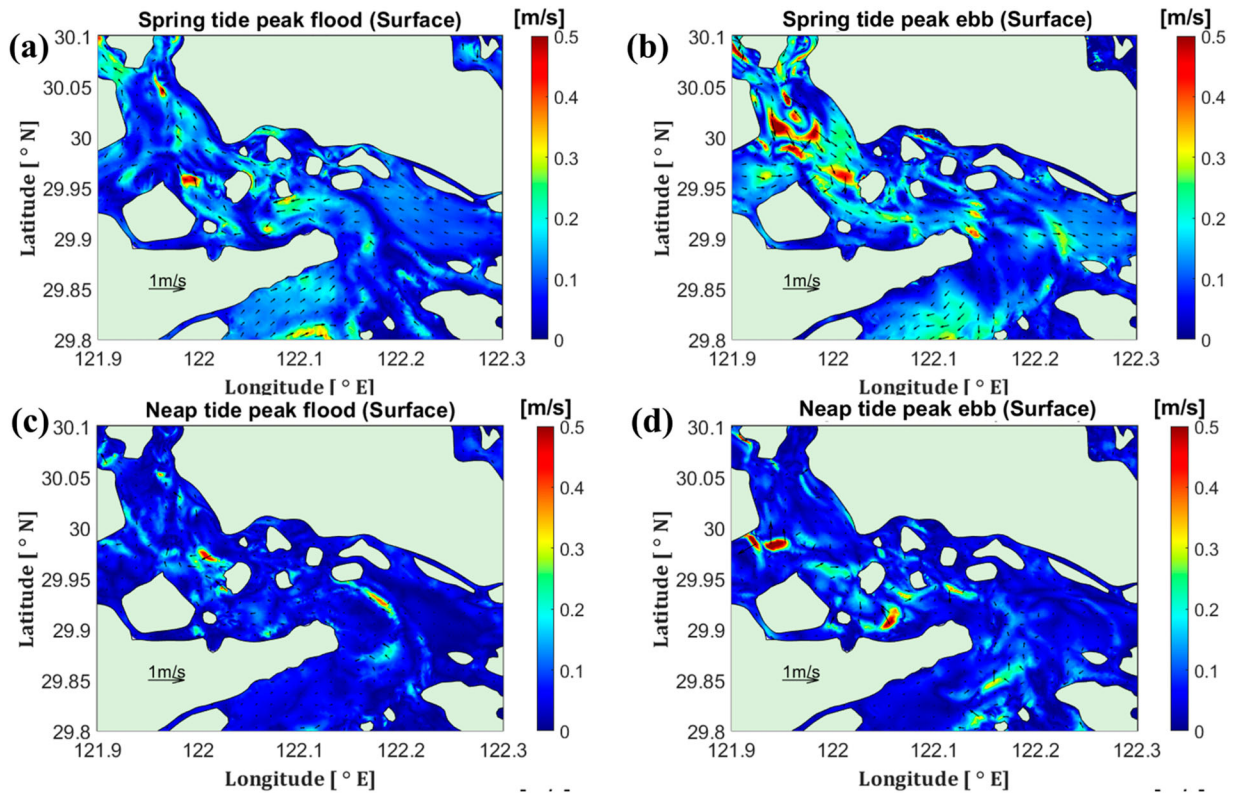
Figure 13. Velocity differences during spring/neap tides, between the model results with and without sediments (test 2-test 1).

4.3. Impacts of SSC on lateral currents

For analyzing the generating mechanisms of the lateral circulation, we show the time series of momentum terms (the term of the equation 1 in the supplementary file) at the station W (the middle of section S2, the high velocity area of the channel) during spring and neap tides (Figure 15).

At the peak flood during the spring tide, the nonlinear advection has a positive (southward) accelerating effect on the middle and lower water, and the negative (northward) accelerating effect on the upper water, which promotes the formation of the clockwise lateral circulation (Figure 15(a, a')). The effect of centrifugal force is similar to that of nonlinear circulation, but the effect is slightly smaller (Figure 15(c, c')). For the Coriolis force, during the flood tide, the acceleration of the middle layer of water is southward, and the acceleration of the upper and lower layers is northward. During the ebb tide, the upper water is northward and the lower water is southward (Figure 15(b, b')). The effect of the baroclinic gradient force is similar to that of the Coriolis force, causing the upper water to accelerate southward during flood tides, and the lower water to accelerate northward. The reverse pattern occurs during the ebb tides (Figure 15(d, d')). The baroclinic gradient force is related to the water density. Therefore, the impact of baroclinic gradient force is enhanced in test 2 when considers sediment.

At the peak flood and ebb tides, the flow velocity is large, hence, the friction dissipation is relatively large. The upper water and lower water have opposite acceleration due to friction dissipation, resulting in lateral circulation (Figure 15(e, e')). Under the combined action of various forces, the lateral circulation of water changes temporally clockwise and anticlockwise. Nonlinear circulation, centrifugal force and baroclinic gradient force are the dominant factors, while the effects of frictional dissipation and Coriolis force are small. On the one hand, the existence of sediment changes the density of the water body and enhances the role of various acceleration terms (except friction dissipation). On the other hand, the friction dissipation term is greatly reduced due to the drag reduction of the bottom fluid mud layer (Figure 15(f, f')).

During the spring and neap tides, we estimate the contribution of the momentum terms to the lateral circulation at the S2 section (Figure 16). If considering sediment in the model in test 2, the frictional dissipation term, nonlinear advection term and baroclinic gradient force term make the main contribution, while Coriolis force and centrifugal force term are very small. The contribution of baroclinic gradient force during neap tides is greater than that during spring tides, and the contribution of nonlinear advection term is smaller during neap tides than that during spring tide. The presence of sediment in
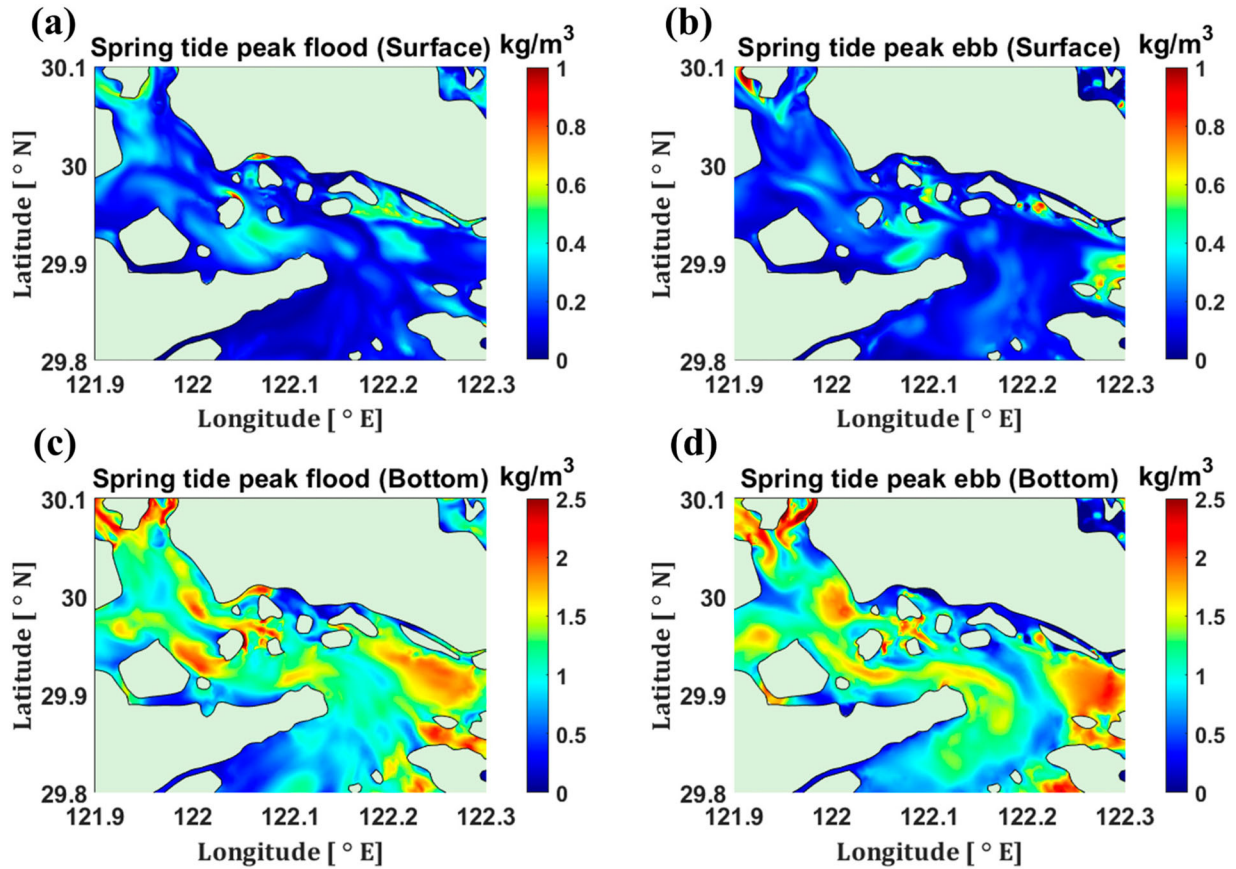
Figure 14. Impacts of sediments on water residual density. Density differences between the model results with and without sediments (test 2-test 1), that is, the change of water density caused by sediment in the DNC during spring/neap tides.

test 2 makes the proportion of centrifugal force term significantly increase, while Coriolis force term is still very small. The presence of sediment reduces the shear stress of the sea bed, thereby increasing the flow velocity and lateral circulation. Figure 16 also illustrates the similar conclusions. The presence of sediment reduces the friction term and nonlinear advection term at each time of the tidal cycle.

In general, frictional dissipation plays an important role in the formation of lateral circulation. Friction modifies the structure, strength, and phase of curvature-induced lateral circulation (Cheng, 2023). The presence of sediment enhances the role of centrifugal force, thus increasing the lateral circulations and sediment fluxes.

5. Conclusions

The three-dimensional tidal dynamics in a macro-tidal turbid deep navigational channel (DNC) in Zhoushan Islands were observationally studied by field data and numerically examined using FVCOM. The impacts of high turbidity on tidal dynamics are numerically investigated. Model results indicate that tidal flow in the Luotou Channel is characterized by the spatially asymmetric tidal elevation and currents. During spring tides, tidal elevation decreases by up to 30 cm at high slack water when tides propagate through the channel. The difference in sea surface elevations, between the seaward side and the landward side of the DNC, reaches 40 cm during the peak flood current. The tidal current directions are controlled by the coastlines. The velocity of ebb tides is higher than that of flood tides. The main tidal channel is near the southern part of DNC during ebb tides, while is near the northern bank during flood tides. The flow channel at the seaward entrance of the DNC is more curved at the bottom level than that at the surface during both peak flood and ebb current. During the flood tides, lateral circulation appears in section S2, with surface currents towards the northern bank and bottom currents towards the southern bank. During the ebb tides, lateral circulation appears in section S3, with surface currents towards the southern bank and bottom currents towards the northern bank. Residual-current speeds peak at about 0.7 m s^{-1} at the northern side of the middle channel and at the northern side of the Chuanshan Peninsula. Two eddies, with vertically averaged current speed of 0.5 m s^{-1}, are generated by the multiple-island geometry, the curvature of the Chuanshan Peninsula
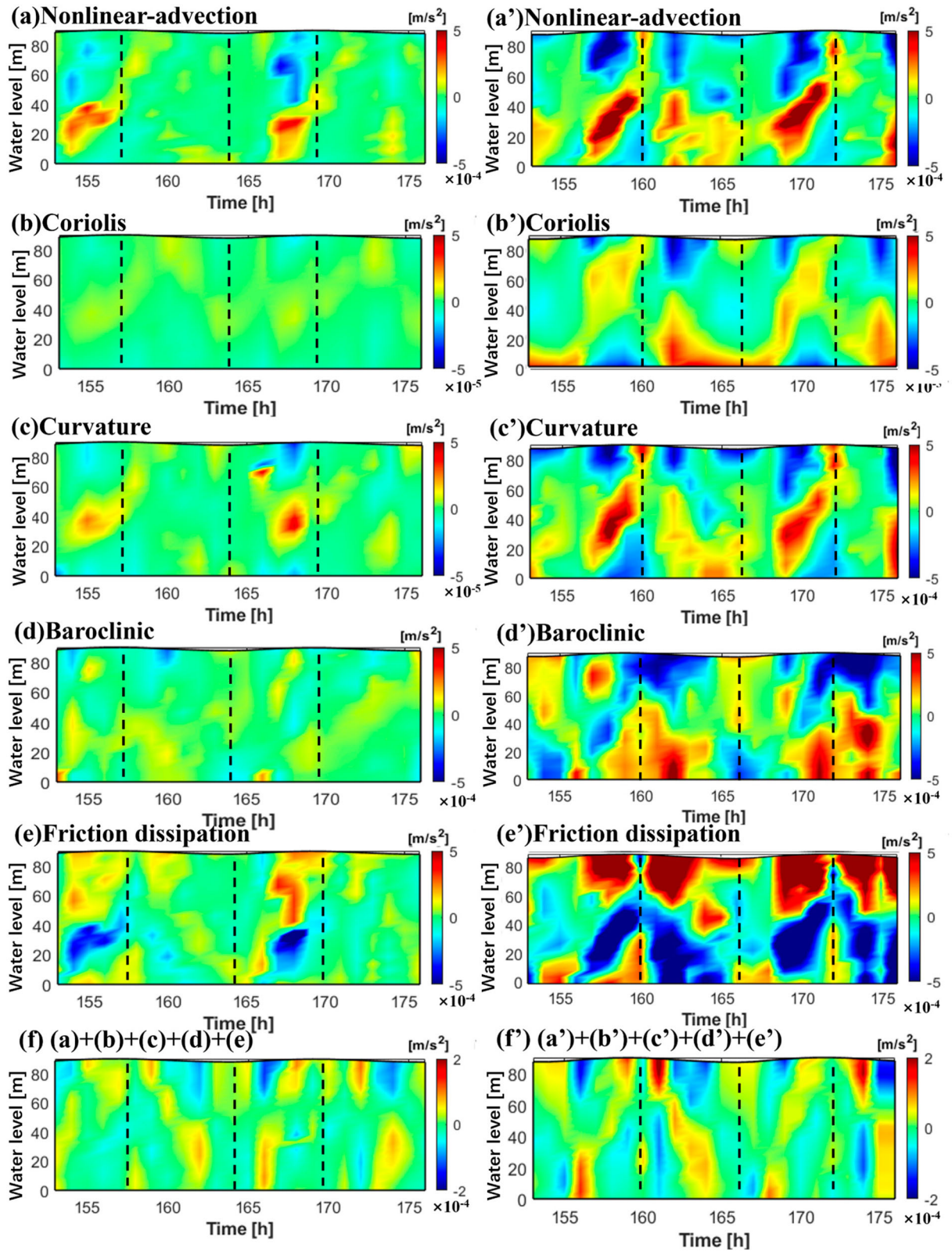
Figure 15. Time series of the momentum terms in the equation (1) in the supplementary file at Station W during spring tide, without (left column) and with (right column) sediment.
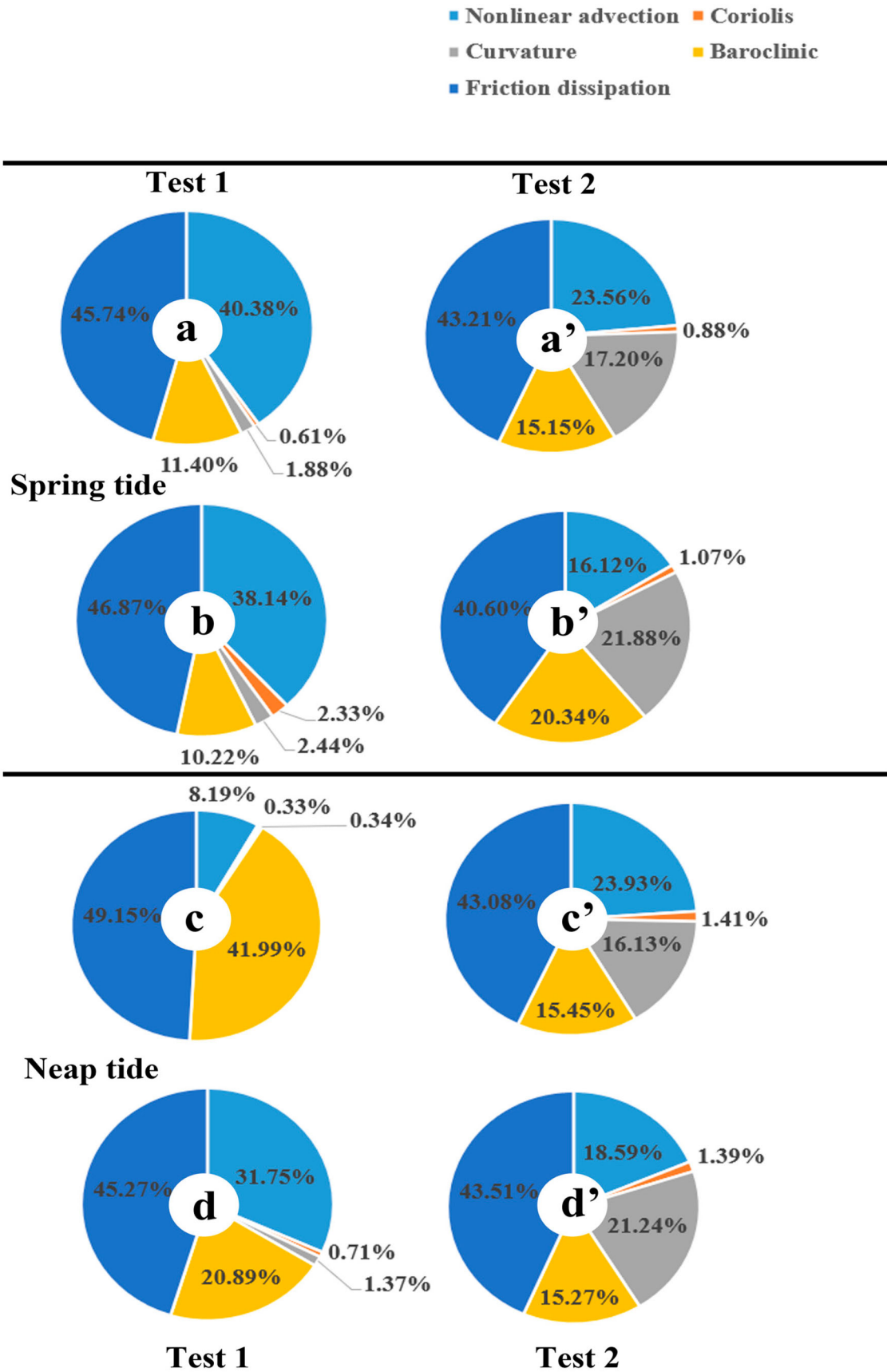
Figure 16. Proportions of momentum terms at Sections S2 during the spring and neap tides with/without sediment. (a, a') flood tide during the spring tide, (b, b') ebb tide during the spring tide, (c, c') flood tide during the neap tide, (d, d') ebb tide during the neap tide.

and the spatially asymmetry of the flooding-ebbing currents. In the four sections the directions of residual currents in the upper and lower water bodies is inconsistent. This pattern is produced by the unbalanced Coriolis force, centrifugal force, sea-level gradient, temperature gradient and salinity gradient in the vertical profile along the channel during both spring and neap tides.

The suspended sediment concentration is impacted by the curvature in DNC, through impacting the hydrodynamics, and there are two high turbidity zones. The high turbidity zones are more northward at flooding tides and more southward at ebbing tides. The distribution of sediment flux is similar to that of residual current. Sediments increase the current velocity through baroclinic gradient force caused by water density and drag reduction effect of mud layer in sea bed. Drag reduction effect of fluid mud is the main effect of increasing flow velocity. At the peak flood and ebb tides, the larger flow velocity enhances the effects of the nonlinear advection, centrifugal force and friction dissipation, and then amplifies the lateral circulation. The asymmetric distribution of currents and SSC leads to the variation of water density to produce baroclinic gradient force. The friction dissipation, followed by nonlinear advection and baroclinic gradient force, dominate the lateral circulation. The presence of sediment increases the effect of centrifugal force, and increases/decrease the contribution of baroclinic gradient force during spring/neap tides.

Disclosure statement

No potential conflict of interest was reported by the author(s).

References

Byun, D. S., Wang, X. H., & Holloway, P. E. (2004). Tidal characteristic adjustment due to dyke and seawall construction in the Mokpo Coastal Zone, Korea. *Estuarine, Coastal and Shelf Science*, 59(2), 185–196. https://doi.org/10.1016/j.ecss.2003.08.007

Calil, P. H. R., Richards, K. J., Jia, Y., & Bidigare, R. R. (2008). Eddy activity in the lee of the Hawaiian Islands. *Deep Sea Research Part II: Topical Studies in Oceanography*, 55(10–13), 1179–1194. https://doi.org/10.1016/j.dsr2.2008.01.008

Cancino, L., & Neves, R. (1999). Hydrodynamic and sediment suspension modelling in estuarine systems: Part II: Application to the Western Scheldt and Gironde estuaries. *Journal of Marine Systems*, 22(2-3), 117–131. https://doi.org/10.1016/S0924-7963(99)00036-6

Cao, Z., & Wang, Y. (1994). *Hydrodynamic sediment numerical simulation*. Tianjin University Press.

Chen, C., Liu, C. H., & Beardsley, R. C. (2003). An unstructured, finite-volume, three-dimensional, primitive equation ocean model: Application to coastal ocean and estuaries. *Journal of Atmospheric and Oceanic Technology*, 20(1), 159–186. https://doi.org/10.1175/1520-0426(2003)020 < 0159:AUGFVT > 2.0.CO;2

Chen, J., Liu, C., Zhang, C., & Walker, H. (1990). Geomorphological development and sedimentation in Qiantang Estuary and Hangzhou Bay. *Journal of Coastal Research*, 6(3), 559–572.

Cheng, P. (2007). *Modeling sediment transport in estuarine environment: Effects of tidal asymmetry, lateral circulation and sediment-induced stratification*. State University of New York at Stony Brook.

Cheng, P. (2023). Lateral circulation in an elongated curved tidal channel. *Journal of Physical Oceanography*, 53(4), 1183–1198. https://doi.org/10.1175/JPO-D-22-0192.1

Choo, H.-S., & Kim, D.-S. (2013). Tide and tidal currents around the archipelago on the southern waters of the South Sea, Korea. *Journal of the Korean Society of Marine Environment and Safety*, 19(6), 582–596. https://doi.org/10.7837/kosomes.2013.19.6.582

Chu, D., Niu, H., Wang, Y., Cao, A., Li, L., Du, Y., & Zhang, J. (2022). Numerical study on tidal duration asymmetry and shallow-water tides within multiple islands: An example of the Zhoushan Archipelago. *Estuarine Coastal and Shelf Science*, 262, 107576.

Dai, Z., Chu, A., Li, W., Li, J., & Wu, H. (2013). Has suspended sediment concentration near the mouth bar of the Yangtze (Changjiang) Estuary been declining in recent years? *Journal of Coastal Research*, 29(4), 809–818. https://doi.org/10.2112/JCOASTRES-D-11-00200.1

Du, Y., Wang, D., Zhang, J., Wang, Y., & Fan, D. (2021). Estimation of initial conditions for surface suspended sediment simulations with the adjoint method: A case study in Hangzhou Bay. *Continental Shelf Research*, 227, 104526.

Du, Z., Yu, Q., Peng, Y., Wang, L., Lin, H., Wang, Y., & Gao, S. (2022). The formation of coastal turbidity maximum by tidal pumping in well-mixed inner shelves. *Journal of Geophysical Research: Oceans*, 127(4), e2022JC018478.

Egbert, G., Bennett, A., & Foreman, M. (1994). Topex/Poseidon tides estimated using a global inverse model. *Journal of Geophysical Research-Oceans*, 99(C12), 24821–24852.

Feng, S., & Yao, Y. (2013). Research on the suspended sediment simulation for the Luotou strait of Zhoushan Islands are. *Marine Science Bulletin*, 32(01), 58–65.

Gusti, G. N. N., Kawanisi, K., Al Sawaf, M. B., Khadami, F., & Xiao, C. (2023). Investigating tidal river dynamics in a longitudinally varying channel geometry. *Continental Shelf Research*, 253, 104901. https://doi.org/10.1016/j.csr.2022.104901

Isoguchi, O., Shimada, M., Sakaida, F., & Kawamura, H. (2009). Investigation of Kuroshio-induced cold-core eddy trains in the lee of the Izu Islands using high-resolution satellite images and numerical simulations. *Remote Sensing of Environment*, 113(9), 1912–1925. https://doi.org/10.1016/j.rse.2009.04.017

Jiang, X., Lu, B., & He, Y. (2013). Response of the turbidity maximum zone to fluctuations in sediment discharge from river to estuary in the Changjiang Estuary (China). *Estuarine, Coastal and Shelf Science*, 131(0), 24–30. https://doi.org/10.1016/j.ecss.2013.07.003

Kim, Y. H., & Voulgaris, G. (2008). Lateral circulation and suspended sediment transport in a curved estuarine channel: Winyah Bay, SC, USA. *Journal of Geophysical Research: Oceans*, 113(C9), C09006. https://doi.org/10.1029/2007jc004509

Li, L., Li, Z., He, Z., Yu, Z., & Ren, Y. (2022). Investigation of storm tides induced by super typhoon in macrotidal Hangzhou Bay. *Frontiers in Marine Science*, 9, 890285. https://doi.org/10.3389/fmars.2022.890285

Li, L., Wang, J., Zheng, Y., Yao, Y., & Guan, W. (2023). Fluid Mud dynamics and Its correlation to hydrodynamics in jiaojiang river estuary, China. *Ocean Science Journal*, 58(1), 8. https://doi.org/10.1007/s12601-023-00102-5

Mitchell, S. B. (2013). Turbidity maxima in four macrotidal estuaries. *Ocean & Coastal Management*, 79, 62–69. https://doi.org/10.1016/j.ocecoaman.2012.05.030

Pan, C., Zheng, J., Chen, G., He, C., & Tang, Z. (2019). Spatial and temporal variations of tide characteristics in Hangzhou Bay and cause analysis. *The Ocean Engineering*, 37((03|3)), 1–11.

Postacchini, M., Manning, A. J., Galantoni, J., Smith, J. P., & Brocchini, M. (2023). A storm driven turbidity maximum in a microtidal estuary. *Estuarine, Coastal and Shelf Science*, 288, 108350. https://doi.org/10.1016/j.ecss.2023.108350

Shi, Z. (1998). Acoustic observations of fluid mud and interfacial waves, Hangzhou Bay, China. *Journal of Coastal Research*, 14(4), 1348–1353.

Tao, J., & Zhu, R. (2022). Exploring the three-dimensional flow-sediment dynamics and trapping mechanisms in a curved estuary: The role of salinity and circulation. *Frontiers in Marine Science*, 9, 76332.

Wang, J. Y., Dijkstra, Y. M., & de Swart, H. E. (2022). Turbidity maxima in estuarine networks: Dependence on fluvial sediment input and local deepening/narrowing with an exploratory model. *Frontiers in Marine Science*, 9. https://doi.org/10.3389/fmars.2022.940081

Wang, S., He, Z., Gu, H., & Xia, Y. (2022). The "two-step" yielding process of the natural mud under steady and oscillatory shear stress. *Frontier in Earth Science*, 10, 1010710. https://doi.org/10.3389/feart.2022.1010710

Wang, X. (2002). Tide-induced sediment resuspension and the bottom boundary layer in an idealized estuary with a muddy bed. *Journal of Physical Oceanography*, 32(11), 3113–3131. https://doi.org/10.1175/1520-0485(2002)032 < 3113:TISRAT > 2.0.CO;2

Wang, X., Byun, D. S., Wang, X., & Cho, Y. K. (2005). Modelling tidal currents in a sediment stratified idealized estuary. *Continental Shelf Research*, 25(5–6), 655–665. https://doi.org/10.1016/j.csr.2004.10.013

Wei, Z., Jiao, X., Du, Y., Zhang, J., Pan, H., Wang, G., Wang, D., & Wang, Y. (2023). The temporal variations in principal and shallow-water tidal constituent and their application in tidal level calculation: An example in Zhoushan Archipelagoes with complex bathymetry. *Ocean & Coastal Management*, 237, 106516. https://doi.org/10.1016/j.ocecoaman.2023.106516

Winant, C. D. (2007). Three-dimensional tidal flow in an elongated, rotating basin. *Journal of Physical Oceanography*, 37(9), 2345–2362. https://doi.org/10.1175/JPO3122.1

Winterwerp, J. C. (2001). Stratification effects by cohesive and noncohesive sediment. *Journal of Geophysical Research: Oceans*, 106(C10), 22559–22574. https://doi.org/10.1029/2000JC000435

Wu, H., Tang, J., Li, W., Xing, F., Yang, H., Zhang, F., & Wang, Y. (2023). Fluid mud induced by periodic tidal advection and fine-grained sediment settling in the Yangtze estuary. *Frontiers in Marine Science*, 10, 1323692. https://doi.org/10.3389/fmars.2023.1323692

Wu, R., Jiang, Z., & Li, C. (2018). Revisiting the tidal dynamics in the complex Zhoushan Archipelago waters: A numerical experiment. *Ocean Modelling*, 132, 139–156. https://doi.org/10.1016/j.ocemod.2018.10.001

Xiao, Z., Wang, X. H., Moninya, R., & Daniel, H. (2019). Numerical modelling of the Sydney harbour estuary, New South Wales: Lateral circulation and asymmetric vertical mixing. *Estuarine, Coastal and Shelf Science*, 217, 132–147. https://doi.org/10.1016/j.ecss.2018.11.004

Yao, Y., Chen, X., Yuan, J., Li, L., & Guan, W. (2023). Impacts of channel dredging on hydrodynamics and sediment dynamics in the main channels of the Jiaojiang River Estuary in China. *Acta Oceanologica Sinica*, 42(9), 132–144. https://doi.org/10.1007/s13131-022-2118-x

Yu, Q., Wang, Y., Gao, J., Gao, S., & Flemming, B. (2014). Turbidity maximum formation in a well-mixed macrotidal estuary: The role of tidal pumping. *Journal of Geophysical Research: Oceans*, 119(11), 7705–7724. https://doi.org/10.1002/2014JC010228

Zheng, J., Xia, X., Lu, S., & Cao, Z. (2022). High-resolution observations of lateral circulation at an inflection bend of the Oujiang River Estuary, China. *Estuarine, Coastal and Shelf Science*, 274(5), 107928. https://doi.org/10.1016/j.ecss.2022.107928

Zhou, X., Dai, Z., & Mei, X. (2020). The multi-decadal morphodynamic changes of the mouth bar in a mixed fluvial-tidal estuarine channel. *Marine Geology*, 429, 106311. https://doi.org/10.1016/j.margeo.2020.106311